


Automated Discovery of Autonomous Quantum Error Correction Schemes

Zhaoyou Wang^{1,*}, Taha Rajabzadeh², Nathan Lee¹ and Amir H. Safavi-Naeini^{1,†}

¹*E. L. Ginzton Laboratory and the Department of Applied Physics, Stanford University, Stanford, California 94305, USA*

²*Department of Electrical Engineering, Stanford University, Stanford, California 94305, USA*

 (Received 11 August 2021; revised 4 December 2021; accepted 7 March 2022; published 4 April 2022)

We can encode a qubit in the energy levels of a quantum system. Relaxation and other dissipation processes lead to decay of the fidelity of this stored information. Is it possible to preserve the quantum information for a longer time by introducing additional drives and dissipation? The existence of autonomous quantum error correcting codes answers this question in the positive. Nonetheless, discovering these codes for a real physical system, i.e., finding the encoding and the associated driving fields and bath couplings, remains a challenge that has required intuition and inspiration to overcome. In this work, we develop and demonstrate a computational approach based on adjoint optimization for discovering autonomous quantum error correcting codes given a Hamiltonian description of a physical system. We implement an optimizer that searches for a logical subspace and control parameters to better preserve quantum information. We demonstrate our method on a system of a harmonic oscillator coupled to a lossy qubit, and find that varying the Hamiltonian distance in Fock space—a proxy for the control hardware complexity—leads to discovery of different and new error correcting schemes. We discover what we call the $\sqrt{3}$ code, realizable with a Hamiltonian distance $d = 2$, and propose a hardware-efficient implementation based on superconducting circuits.

DOI: [10.1103/PRXQuantum.3.020302](https://doi.org/10.1103/PRXQuantum.3.020302)

I. INTRODUCTION

Physical qubits always live in noisy environments, which leads to decoherence and hinders the development of scalable quantum computers. Quantum error correction (QEC) solves this problem by encoding logical states in a way that errors caused by the environment can be detected and corrected without accessing the encoded quantum information [1]. The standard implementation of QEC involves error syndrome measurements followed by adaptive recovery operations [1], with the drawback of introducing additional errors caused by imperfect measurements [2–4] and significant hardware overhead associated with the real-time classical feedback [5,6]. In contrast, autonomous quantum error correction (AQEC) circumvents the necessity of classical adaptive control by embedding the active measurement and feedback processes into the passive internal dynamics of the system [7–11]. With

an engineered interaction between the qubit and a lossy ancilla, accumulated entropy in the qubit due to physical errors can be coherently transferred to the ancilla in real time and then evacuated through ancilla decay [7,9,10]. A fault-tolerant architecture may benefit from elements with AQEC that are combined together to implement a standard QEC protocol—AQEC operating in the few-qubit regime could reduce the overhead for standard QEC.

An experimental platform will feature limited hardware control and more complex errors, which sometimes deviate from the assumptions underlying many QEC codes. Designing the optimal platform-specific QEC scheme is therefore highly nontrivial and will likely require a numerical approach that takes into account the hardware constraints. In this direction [12–15], it has been shown that the encoding and decoding operations can be adapted to a given error channel via iterative convex optimization [13, 15], assuming arbitrary operations are achievable. More recently, quantum-gate-based methods were developed to incorporate certain features at the physical level, including the available gate set and qubit connectivity [16,17]. It is important to extend these approaches to take into account decoherence during the gate operation and measurements, as well as any coherent leakage out of the qubit computational subspace [18]. AQEC, on the other hand, requires only Hamiltonian dynamics and ancilla relaxation

*zhaoyou@stanford.edu

†safavi@stanford.edu

Published by the American Physical Society under the terms of the [Creative Commons Attribution 4.0 International license](https://creativecommons.org/licenses/by/4.0/). Further distribution of this work must maintain attribution to the author(s) and the published article's title, journal citation, and DOI.

to preserve the quantum information. Therefore, automated discovery of AQEC schemes naturally incorporates the native device Hamiltonian and decay channels, bringing it closer to experimental deployment.

Our paper is organized as follows. In Sec. II, we develop a numerical framework (AutoQEC) for automatically designing AQEC schemes for a given experimental platform. AutoQEC aims to discover strategies that preserve the encoded quantum information by optimizing over the logical states and control parameters. In Sec. III, we demonstrate AutoQEC on a system consisting of a single bosonic mode coupled to a lossy qubit, and find that the resulting AQEC scheme depends on the constraints on the system, such as dissipation channels and Hamiltonian connectivity. In Sec. IV, we propose a circuit implementation of the discovered AQEC scheme and in Sec. V we conclude our discussion with potential directions for future works.

II. AUTOQEC FRAMEWORK

Our method is illustrated in Fig. 1(a) where the physical system is described by a parametrized Hamiltonian $\hat{H}(\alpha) = \sum_{j=1}^N \alpha_j \hat{H}_j$ and a set of Lindblad dissipators $\{D[\sqrt{\beta_k} \hat{A}_k], k = 1, \dots, K\}$, where $D[\hat{A}](\hat{\rho}) = \hat{A} \hat{\rho} \hat{A}^\dagger - \frac{1}{2} \{\hat{A}^\dagger \hat{A}, \hat{\rho}\}$. Here $\alpha = \{\alpha_j\}$, $\beta = \{\beta_k\}$ are the control parameters while $\{\hat{H}_j\}$ and $\{\hat{A}_k\}$ represent the available control Hamiltonians and decay channels in the system. The

quantum dynamics follows the master equation:

$$\dot{\hat{\rho}} = -i[\hat{H}(\alpha), \hat{\rho}] + \sum_{k=1}^K \beta_k \left(\hat{A}_k \hat{\rho} \hat{A}_k^\dagger - \frac{1}{2} \{ \hat{A}_k^\dagger \hat{A}_k, \hat{\rho} \} \right). \quad (1)$$

Learning a logical qubit is equivalent to finding a two-dimensional subspace that is well-protected under the dynamics of Eq. (1). More concretely, starting from an arbitrary point on the Bloch sphere spanned by basis vectors $|\psi_0\rangle$ and $|\psi_1\rangle$ as the initial state [Fig. 1(a)]

$$|\psi_{\theta\phi}\rangle = \cos \frac{\theta}{2} |\psi_0\rangle + e^{i\phi} \sin \frac{\theta}{2} |\psi_1\rangle, \quad (2)$$

the fidelity $F_{\theta\phi} = \langle \psi_{\theta\phi} | \hat{\rho}_{\theta\phi} | \psi_{\theta\phi} \rangle$ characterizes how much information is preserved for $|\psi_{\theta\phi}\rangle$, where $\hat{\rho}_{\theta\phi}$ is the state at some later time T evolved under Eq. (1). By integrating the single-state fidelity over the Bloch sphere Ω , the average fidelity of the logical subspace is defined as

$$\bar{F}(\alpha, \beta, |\psi_0\rangle, |\psi_1\rangle) \equiv \frac{1}{4\pi} \int_{\Omega} F_{\theta\phi} d\Omega. \quad (3)$$

Maximizing \bar{F} under the orthogonality constraints $|\langle \psi_0 | \psi_1 \rangle| = 0$ leads to discovery of AQEC schemes. Notice that by definition \bar{F} is invariant under arbitrary rotations within the logical subspace, therefore $|\psi_0\rangle$ and $|\psi_1\rangle$ are not unique for a given encoding.

We found that using \bar{F} as the objective function in AutoQEC is sometimes ill conditioned and leads to an untenable optimization landscape with high sensitivity to the parameters. This can be understood by considering how a small change in the energy levels can cause a phase to build up over the evolution time and make the fidelity fluctuate rapidly with the optimization parameters. Our solution was to find the best overlap modulo a Z rotation in the logical subspace (see Appendix B 1). A similar but even less constraining approach has been used previously where the recoverable quantum information is maximized [16].

Optimization of the average fidelity \bar{F} is in general a high-dimensional nonconvex problem, and local gradient information could potentially accelerate the search of good solutions. The gradients of \bar{F} with respect to the logical states $\{|\psi_0\rangle, |\psi_1\rangle\}$ and the control parameters $\{\alpha, \beta\}$ can be calculated with the adjoint method [19,20], a technique for efficiently backpropagating gradients through an ordinary differential equation (ODE). Mathematically, considering a state v obeying the ODE $\dot{v} = f(v, \theta)$ with parameter θ and a loss function $L[v(T)]$ depending on the final state at time T , the key quantity introduced in the adjoint method is the adjoint state $a(t) = \partial L / \partial v(t)$ whose dynamics satisfies $\dot{a} = -(\partial f / \partial v) a$ [Fig. 1(b)]. Therefore, the gradient

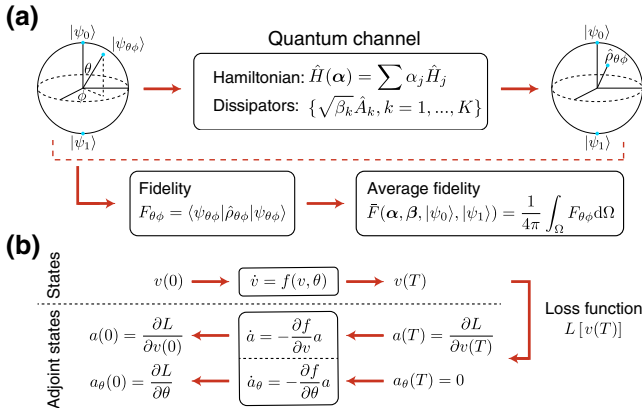


FIG. 1. Schematic of the average fidelity and the adjoint method. (a) An arbitrary state $|\psi_{\theta\phi}\rangle$ on the Bloch sphere is mapped to a density matrix $\hat{\rho}_{\theta\phi}$ by a quantum channel described by a set of control Hamiltonians and dissipators. Averaging the single-state fidelity $F_{\theta\phi}$ over the Bloch sphere gives the average fidelity \bar{F} . (b) A loss function $L[v(T)]$ depending on the final state $v(T)$ of an ODE will implicitly be a function of the initial state $v(0)$ and the ODE parameter θ . The gradients of L with respect to $v(0)$ and θ can be computed by integrating the adjoint equations backward in time.

of L with respect to the initial state $a(0) = \partial L / \partial v(0)$ can be computed by starting from $a(T) = \partial L / \partial v(T)$ and integrating the adjoint equation backward in time. Similarly, the gradient with respect to the ODE parameter θ can be computed by solving another adjoint equation $\dot{a}_\theta = -(\partial f / \partial \theta)a$ backward in time starting from $a_\theta(T) = 0$ [Fig. 1(b)]. Notice that even though we use scalar notations here for simplicity, the results above can be easily generalized to the vector case (see Appendix A).

III. BOSONIC CODE DISCOVERY

We use `AutoQEC` to study autonomous implementations of bosonic codes [2,3,9,21–24], motivated by their advantages of hardware efficiency and simplified error models over the traditional qubit-based QEC [1,5,25]. The system consists of a single harmonic oscillator as the storage mode of quantum information coupled to a lossy ancilla qubit for entropy evacuation [Fig. 2(a)], and the dissipators are $D[\sqrt{\kappa} \hat{a}]$ and $D[\sqrt{\kappa_q} \hat{b}]$ where \hat{a} is the annihilation operators for the bosonic mode and $\hat{b} = |g\rangle\langle e|$ with $g(e)$ representing the ancilla qubit in its ground (excited) state. We choose the basis states of the joint system as $|n, g(e)\rangle$ where n is the index of the Fock state with a cutoff at 20. During the optimization of \bar{F} , only the logical states $\{|\psi_0\rangle, |\psi_1\rangle\}$ and the Hamiltonian parameters

α are updated while the loss rates are fixed at $\kappa/2\pi = 0.1$ MHz and $\kappa_q/2\pi = 20$ MHz. We choose a total evolution time $T = 0.5 \mu\text{s}$, and bound the driving strength of each Hamiltonian by $|\alpha_j|/2\pi \leq 10$ MHz reflecting what we consider as realistic coupling rates. With such constraints, a Fock state cutoff of 20 is more than enough since physically larger photon-number states decay more quickly and require stronger driving to protect.

We begin by considering Hamiltonians with all-to-all coupling in the Hilbert space [Fig. 2(b)] where the control Hamiltonians $\{\hat{H}_j\}$ include couplings between any two basis states $\{|m, g(e)\rangle\langle n, g(e)|\}$. Running the `AutoQEC` optimizer on this problem leads repeatedly to codes such as those shown in Fig. 2(b)i and ii. In both cases, we plot the Wigner function of the maximally mixed state $\hat{\rho}_{\text{code}} = \frac{1}{2}(|\psi_0\rangle\langle\psi_0| + |\psi_1\rangle\langle\psi_1|)$ as a basis-independent representation of the logical subspace [24]. The two logical subspaces are basically equivalent to each other up to a random displacement and rotation in phase space. Moreover, the code in Fig. 2(b)i is almost identical ($F \equiv 2\text{Tr}[\hat{\rho}_1\hat{\rho}_2] \approx 99.4\%$, where $\hat{\rho}_1$ and $\hat{\rho}_2$ are the two codes) with the $\sqrt{17}$ code [23,24], which is the smallest code in photon number that allows exact correction of a single-photon-loss error. The time evolution of the average fidelity quantifies the AQEC performance. We plot this for both resulting codes [Fig. 2(e) blue solid and dashed lines], and see that it exceeds the break-even fidelity [Fig. 2(e) gray shaded region boundary] defined as the average fidelity for the trivial $|0\rangle$ and $|1\rangle$ encoding with $\hat{H} = 0$:

$$\bar{F}(t) = \frac{1}{6} (e^{-\kappa t} + 2e^{-\kappa t/2} + 3). \quad (4)$$

Exceeding the break-even fidelity indicates that quantum information encoded in the logical subspace is preserved longer than the lifetime of any individual physical element.

To avoid the significant experimental challenge of implementing an all-to-all Hamiltonian for a harmonic oscillator, we consider a more realizable restricted set of control Hamiltonians containing only terms $\{|m, g\rangle\langle n, e|\}$ (and the conjugates) where $0 < |m - n| \leq d$ and the distance $d = 2$ [Fig. 2(c)]. We choose such a restriction since we expect interaction terms such as $\hat{a}^\dagger \hat{b}$ and $\hat{a}^{\dagger 2} \hat{b}$ to be selectively realizable by engineering the drive frequencies given large dispersive couplings (see implementation details below). We also avoid coupling terms like $\{|m, g\rangle\langle n, g|\}$ and $\{|m, e\rangle\langle n, e|\}$ since *independently* engineering them for a linear system \hat{a} is difficult as we no longer have access to the dispersive nonlinearity. Over many runs of `AutoQEC`, we discover two different types of results that exceed break even. Figure 2(c)i shows the logical subspace of a discovered bosonic code, which exhibits error correction performance [Fig. 2(e) red solid line] that approaches the all-to-all coupling results. A second

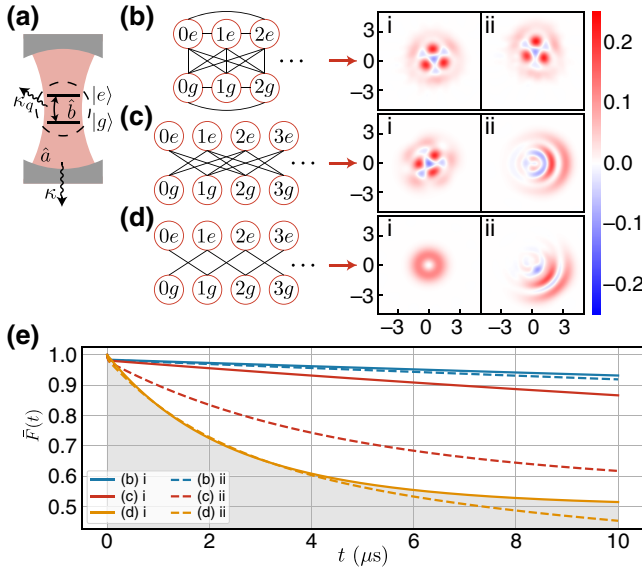


FIG. 2. Optimization results for different Hamiltonian distances. (a) Schematic of a single bosonic mode \hat{a} coupled to a lossy ancilla qubit \hat{b} . (b)–(d) Wigner functions of the discovered codes for all-to-all (b), distance $d = 2$ (c), and $d = 1$ (d) Hamiltonians. Here i and ii are two of the discovered encodings from many runs of `AutoQEC` for each Hamiltonian setting. (e) Average fidelity for all-to-all (blue), $d = 2$ (red), and $d = 1$ (yellow) results. The gray shaded region indicates fidelities below or equal to the break-even point.

encoding shown in Fig. 2(c)ii provides only partial protection in the logical subspace, where $|\psi_0\rangle$ occupies only low photon-number states and $|\psi_1\rangle$ occupies only high photon-number states (see Appendix F). In a way that is reminiscent of recent works on error-biased cat qubits [26], both $|\psi_0\rangle$ and $|\psi_1\rangle$ are preserved by the Hamiltonian with fidelities above break even, but not some of their superpositions (see Appendix F). Nevertheless, the average fidelity of this encoding still exceeds break even [Fig. 2(e) red dashed line].

We fail to discover any error correcting codes with performance beyond break even with a Hamiltonian distance $d = 1$ [Fig. 2(d)]. Most AutoQEC searches end with the $|0\rangle$ and $|1\rangle$ subspace [Fig. 2(d)i], while occasionally we also obtain states [Fig. 2(d)ii] similar to the $d = 2$ case Fig. 2(c)ii, with a fidelity [Fig. 2(e) yellow dashed line] slightly below break even.

The overall efficiency in discovering codes that exceed break even from many runs of AutoQEC depends on the Hamiltonian setting. With all-to-all coupling, the efficiency of finding an encoding like Fig. 2(b)i or ii is about 30%—the remaining 70% of the runs mostly find the trivial $|0\rangle$ and $|1\rangle$ encoding. In the $d = 2$ case, the probability of finding an encoding like Fig. 2(c)i is about 10%, while finding a partially protected qubit like Fig. 2(c)ii is about 20%, with the remaining 70% still converging to the trivial encoding. In the $d = 1$ case, the efficiency is 0 since there is probably no error correction code that can be autonomously protected by a $d = 1$ Hamiltonian. The efficiency of AutoQEC also depends on κT for searching bosonic codes. For $\kappa T \ll 1$, the system goes through transient dynamics and does not have enough time to correct the error after single-photon decay. In this regime, the trivial $|0\rangle$ and $|1\rangle$ encoding actually performs better than doing AQEC. Similar short-term dynamics have been seen in other AQEC approaches [7]. On the other hand, for $\kappa T \gg 1$ any 2D subspace that is not a QEC code will quickly collapse into a single steady state of the Hamiltonian and dissipators, and a maximum average fidelity of 0.5 is almost everywhere in the search space, leading to poor efficiency. We therefore choose an intermediate value of $\kappa T \approx 0.3$ where the dominating error process is single-photon decay.

We further investigate the $d = 2$ code in Fig. 2(c)i. Figure 3 shows two orthogonal code words spanning the logical subspace and the associated Hamiltonian. Inspired by the numerical results [Figs. 3(a) and 3(b)], we analytically derive the logical states as ($F \approx 99.9\%$; see Appendix C)

$$|\psi_0\rangle = \sqrt{1 - \frac{1}{\sqrt{3}}} |0\rangle + \frac{1}{\sqrt{3}} |3\rangle,$$

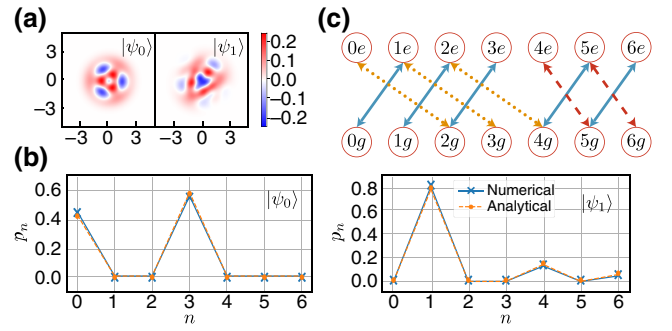


FIG. 3. The $\sqrt{3}$ code. (a) Wigner functions of the two logical basis states from AutoQEC. (b) Photon-number distribution of the analytically derived $\sqrt{3}$ code agrees well with the numerical result, where $|\psi_0\rangle \in \text{span}\{|0\rangle, |3\rangle\}$ and $|\psi_1\rangle \in \text{span}\{|1\rangle, |4\rangle, |6\rangle\}$. (c) Required Hamiltonian couplings for autonomously protecting the code.

$$|\psi_1\rangle = \sqrt{\frac{2(6-\sqrt{3})}{\sqrt{3}+9}} |1\rangle - \sqrt{\frac{(\sqrt{3}-1)(6-\sqrt{3})}{2(\sqrt{3}+9)}} |4\rangle + \sqrt{\frac{3-\sqrt{3}}{2(\sqrt{3}+9)}} |6\rangle \quad (5)$$

and name it the $\sqrt{3}$ code, after the average number of photons in its codewords.

The Hamiltonian found by AutoQEC uses three types of couplings [Fig. 3(c)]: type 1 (blue solid line) $|n-1, g\rangle \leftrightarrow |n, e\rangle$, type 2 (red dashed line) $|n+1, g\rangle \leftrightarrow |n, e\rangle$, and type 3 (yellow dotted line) $|n+2, g\rangle \leftrightarrow |n, e\rangle$. The general form of this Hamiltonian is

$$\hat{H} = \sum_{l=1,2,3} \hat{H}^{(l)}, \quad \hat{H}^{(l)} = \sum_n \alpha_n^{(l)} |n\rangle \langle n+d_l| \otimes \hat{b}^\dagger + \text{h.c.}, \quad (6)$$

where $\hat{H}^{(l)}$ corresponds to the type l couplings with distances $d_1 = -1, d_2 = 1, d_3 = 2$. The effective dissipator for the \hat{a} mode after adiabatically eliminating qubit \hat{b} [27] is $D[|\psi_0\rangle \langle \psi_2| + |\psi_1\rangle \langle \psi_3| + \dots]$, where $|\psi_2\rangle \propto \hat{a} |\psi_0\rangle$ and $|\psi_3\rangle \propto \hat{a} |\psi_1\rangle$ are the error states. The $|\psi_0\rangle \langle \psi_2| + |\psi_1\rangle \langle \psi_3|$ part of the dissipator explains why \hat{H} can correct photon-loss error, while the \dots part is crucial for controlling the distance of \hat{H} without affecting the error correction behavior (see Appendix C). We emphasize that although both logical states and Hamiltonian parameters can be derived and understood analytically for the $\sqrt{3}$ code, the analytical expressions are not needed for the circuit implementation below, and we use only parameters directly from the AutoQEC optimization.

To the best of our knowledge, existing single-mode bosonic codes [21–24] all require high-distance Hamiltonians to protect, which are challenging to engineer experimentally. Therefore, autonomous implementations

of these codes [3,9] instead apply an engineered unitary stroboscopically to correct errors accumulated during some waiting time. The error correction unitary relies on pulse engineering for the low-distance physical Hamiltonians, and effectively realizes the high-distance mapping from the error subspace to the logical subspace. In contrast, the $\sqrt{3}$ code requires only a $d = 2$ Hamiltonian and therefore can operate in the fully autonomous setting [7] where the Hamiltonian itself evacuates entropy continuously from the system, eliminating the need for applying any error correction unitary stroboscopically.

IV. CIRCUIT QED IMPLEMENTATION

Our goal now is to find a physical implementation of the Hamiltonian, Eq. (6), discovered by AutoQEC. In circuit QED, a method for selectively driving such transitions uses off-resonant coupling between a resonator and a nonlinear ancilla qubit circuit to realize a dispersive $\chi \hat{a}^\dagger \hat{a} \hat{b}^\dagger \hat{b}$ interaction. In the presence of this nonlinear level structure, coupling $|m, g\rangle$ and $|n, e\rangle$ together is achieved by driving the system so that the operator $\hat{a}^{m-n} \hat{b}^\dagger$ (if $m > n$, otherwise $\hat{a}^{\dagger(n-m)} \hat{b}^\dagger$) appears in the Hamiltonian, oscillating at frequency $n\chi$ in the rotating frame of both \hat{a} and \hat{b} . This approach requires that the driving strength $|\alpha_j|$ is sufficiently weaker than χ so that a rotating wave approximation (RWA) may be made to drop the undesired couplings. For example, $\hat{H}^{(1)}$ is effectively implemented by $\hat{H}_d^{(1)}(t) = f_1(t) \hat{a}^\dagger \hat{b}^\dagger + \text{h.c.}$ with $f_1(t) = \sum_n \alpha_n^{(1)} e^{-in\chi t} / \sqrt{n}$. Similarly $\hat{H}^{(2)}$ and $\hat{H}^{(3)}$ can be realized by including driving fields that properly modulate the $\hat{a} \hat{b}^\dagger$ and $\hat{a}^2 \hat{b}^\dagger$ terms of the Hamiltonian (see Appendix E).

Before even considering the circuit implementation, we note that the above approach has a serious shortcoming related to how the dispersive nonlinearity modifies the dissipative dynamics. The photon emitted by the relaxation $|n, e\rangle \rightarrow |n, g\rangle$ at frequency ω_n is spaced from $\omega_{n\pm 1}$ by χ [Fig. 4(a)i], which is much larger than the linewidth $\kappa_q \sim |\alpha_j|$ of these emission lines due to the RWA requirement $\chi \gg |\alpha_j|$. Therefore, the emitted photons would leak information about the photon-number distribution and the correct dissipator is no longer $D[\hat{b}]$ for which the code was optimized, but an incoherent sum of terms $D[|n, g\rangle\langle n, e|]$.

We erase the which-way information by including an additional lossy ancillary system and a number of drives with frequencies tuned to overlap the spectrum of emitted photons. This extra lossy qubit \hat{c} does not dispersively couple to \hat{a} —in contrast to qubit \hat{b} , which we also now make long lived as it mediates interaction between the storage mode \hat{a} and the lossy ancilla \hat{c} [Fig. 4(b)]. Let $|e_1\rangle$ and $|e_2\rangle$ be the excited states of qubits \hat{b} and \hat{c} , respectively, the interaction \hat{H}_{bc} between \hat{b} and \hat{c} should quickly transfer any occupation in $|n, e_1\rangle$ caused by a photon-loss error in \hat{a} into $|n, e_2\rangle$, which then relaxes back to $|n, g\rangle$.

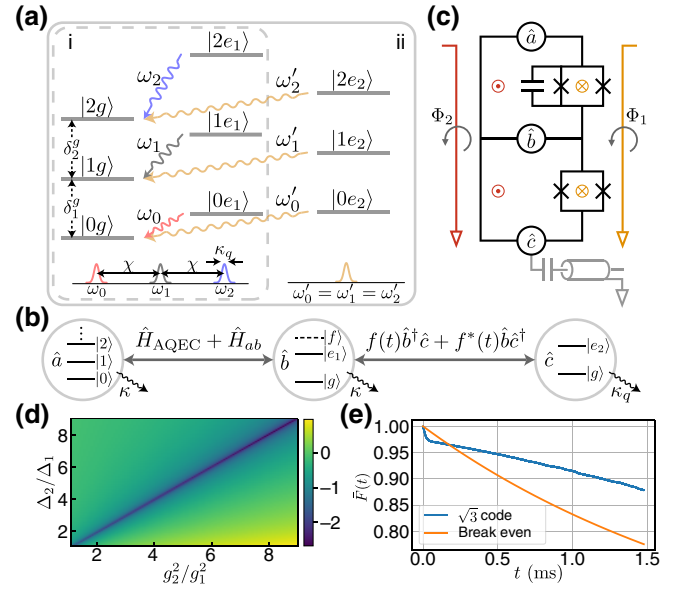


FIG. 4. Circuit implementation of the discovered AQEC scheme. (a) Level diagram and emission spectrum before (i) and after (ii) erasing the which-way information. (b) Schematic interactions within the extended system with an additional lossy qubit \hat{c} . (c) Circuit design that implements the desired interactions by modulating the flux threading the smaller (yellow) and larger (red) loops. (d) $\log_{10} \mathcal{B}$ as a function of g_2^2/g_1^2 and Δ_2/Δ_1 , which is minimized when $g_1^2/\Delta_1 \approx g_2^2/\Delta_2$. The simulation is performed with $\Delta_1/2\pi = 1$ GHz and $g_1/2\pi = 100$ MHz. (e) Average fidelity of the $\sqrt{3}$ code from a time-domain simulation of the full circuit dynamics.

Due to the absence of dispersive coupling, the emitted photon from \hat{c} does not reveal information about the \hat{a} states, which eliminates the which-way information [Fig. 4(a)ii]. Because the transition frequency between $|n, e_1\rangle$ and $|n, e_2\rangle$ depends on n , the desired swapping Hamiltonian $\hat{H}_{bc} = \Omega \sum_n e^{-in\chi t} |n, e_1\rangle \langle n, e_2| + \text{h.c.}$ is time dependent, which can be implemented as $f(t) \hat{b}^\dagger \hat{c} + \text{h.c.}$ with $f(t) = \Omega \sum_n e^{-in\chi t}$ and $\chi \gg \Omega$.

Having incorporated the second ancillary qubit, we propose a superconducting circuit [Fig. 4(c)] that implements the discovered AQEC scheme. The direct capacitive coupling between \hat{a} and \hat{b} gives rise to a linear interaction $g(\hat{a}^\dagger \hat{b} + \hat{a} \hat{b}^\dagger)$, which effectively generates a dispersive coupling $\chi \hat{a}^\dagger \hat{a} \hat{b}^\dagger \hat{b}$ with $\chi = 4g^2/\Delta$ in the large detuning regime $\Delta = |\omega_a - \omega_b| \gg g$ [27,28]. The two superconducting quantum interference devices (SQUIDs) introduce nonlinear interactions of the form $\cos \hat{\phi}_{xy}$ and $\sin \hat{\phi}_{xy}$ where $\hat{\phi}_{xy} = \varphi_x(\hat{x} + \hat{x}^\dagger) + \varphi_y(\hat{y} + \hat{y}^\dagger)$ with $(x, y) = (a, b), (b, c)$. Different terms from the cos and sin Taylor expansions can be selected by parametrically driving the flux threading the circuit loops [7], which realize both the AQEC Hamiltonian between \hat{a} and \hat{b} and the swapping Hamiltonian \hat{H}_{bc} . With proper placement of mode frequencies, the $\hat{a} \leftrightarrow \hat{b}$

and $\hat{b} \leftrightarrow \hat{c}$ couplings can be controlled at very different driving frequencies and only a minimum of two flux lines are required (see Appendix E).

The interaction $g(\hat{a}^\dagger \hat{b} + \hat{a} \hat{b}^\dagger)$ of the proposed circuit implements the needed dispersive coupling at the leading order. However, its higher-order effects induce a Kerr nonlinearity on the \hat{a} mode [29] that can be comparable to κ , causing real deleterious effects on the coherence of the system. Due to this Kerr nonlinearity, when the \hat{a} mode decays from $|n, g\rangle$ to $|n-1, g\rangle$, the emitted photon frequencies $\{\delta_n^g\}$ are not perfectly identical, but rather have a finite bandwidth $\mathcal{B} \equiv \max\{\delta_n^g\} - \min\{\delta_n^g\}$. For realistic parameters where $\mathcal{B} > \kappa$, the environment learns about the photon-number distribution of the resonator, inducing additional dephasing. AutoQEC's assumption of a dissipator $D[\hat{a}]$ is then no longer correct and an incoherent sum of $D[|n-1, g\rangle\langle n, g|]$ more accurately captures the resonator damping process, reducing the fidelity.

Properly addressing parasitic Kerr nonlinearities is a common challenge in bosonic quantum hardware [29]. By leveraging the $|f\rangle$ level of the qubit \hat{b} and engineering the linear coupling between \hat{a} and \hat{b} , we find a way to suppress the emission bandwidth \mathcal{B} by a few orders of magnitude. Consider the Hamiltonian of a harmonic oscillator coupled to a three-level qubit

$$\begin{aligned} \hat{H}_{ab} = & \Delta_1 |e\rangle\langle e| + \Delta_2 |f\rangle\langle f| + g_1 (\hat{a}^\dagger |g\rangle\langle e| + \hat{a} |e\rangle\langle g|) \\ & + g_2 (\hat{a} |f\rangle\langle e| + \hat{a}^\dagger |e\rangle\langle f|). \end{aligned} \quad (7)$$

We find that by judiciously setting the detunings Δ_1 and Δ_2 such that $g_1^2/\Delta_1 \approx g_2^2/\Delta_2$, \mathcal{B} is eliminated to the leading order (see Appendix D). This is also verified numerically in Fig. 4(d) where $\log_{10} \mathcal{B}$ as a function of g_2^2/g_1^2 and Δ_2/Δ_1 is minimized along the diagonal.

Finally, we perform a full quantum simulation of the proposed circuit. Given our choice of g and the detunings, an experimentally realistic $\chi/2\pi \approx 10$ MHz is achieved. To safely satisfy the parameter hierarchy $\chi \gg |\alpha_i| \gg \kappa$, we rescale all control parameters down to $|\alpha_i|/2\pi \approx 10$ kHz with $\kappa/2\pi = 0.1$ kHz and $\kappa_q/2\pi = 20$ kHz, which has the same AQEC performance but at a different time scale. A time-domain simulation of the full circuit dynamics (see Appendix E) proves that the average fidelity for the $\sqrt{3}$ code indeed exceeds the break-even point [Fig. 4(e)], which confirms our circuit design and the AQEC behavior. Notice that the circuit Hamiltonian [Eq. (E6) in Appendix E] assumed in the simulation incorporates the storage mode \hat{a} and both ancilla qubits together with the time-dependent flux drives in the lab frame, and the control parameters α obtained from AutoQEC enter the Hamiltonian as amplitudes of the flux drives. Even though $\kappa/2\pi = 0.1$ kHz is quite demanding experimentally, we expect it to be improved with better circuit designs and proper

compensation of level Stark shifts, and eventually realizable with 3D microwave cavity [30] or quantum acoustic platforms [31,32].

V. DISCUSSION

We have proposed and demonstrated a numerical framework for automated discovery of AQEC schemes. In future works, AutoQEC may be extended into the few logical qubit regime, e.g., learning multiple protected qubits by searching for a higher-dimensional logical subspace with more mutually orthogonal logical basis states, as well as learning quantum gates. This would require speeding up the physical simulation, since computational cost is the main limitation common to any automated approaches based on simulating the actual physical system. It would also be important to incorporate more of the physical layer design, which was done “by hand” in this work, into the optimization algorithm. Finally, applying the adjoint method to other physical systems with the goal of improving quantum simulation, sensing and communications protocols seems within reach.

ACKNOWLEDGMENTS

This work was funded by the U.S. government through the Office of Naval Research (ONR) under Grant No. N00014-20-1-2422, a MURI grant from the U.S. Air Force Office of Scientific Research (Grant No. FA9550-17-1-0002), and the Department of Energy through Grant No. DE-SC0019174. The authors wish to thank NTT Research for their financial and technical support. A.H.S.-N. acknowledges support from the David and Lucille Packard Fellowship, and the Sloan Fellowship.

APPENDIX A: INTRODUCTION TO ADJOINT METHOD

In this section, we provide the general derivation of the adjoint method [19,20] and apply it to the master equation governing the dynamics of a dissipative quantum system.

1. Derivation of the adjoint method

Consider an initial value problem

$$\frac{d\mathbf{v}}{dt} = f(\mathbf{v}, \boldsymbol{\theta}), \quad (\text{A1})$$

where the state \mathbf{v} evolves from $t=0$ to $t=T$ and $\boldsymbol{\theta}$ are the time-independent parameters for the ODE. Here we assume that there is a “loss function” $L[\mathbf{v}(T)]$, which depends only on the final state $\mathbf{v}(T)$. This final state implicitly depends on both the initial state $\mathbf{v}(0)$ and the parameters $\boldsymbol{\theta}$ that specify its time evolution through the integration of the ODE. Our goal is to compute the gradient of L with respect to both the initial state $[\partial L/\partial \mathbf{v}(0)]$ and the ODE

parameters $[\partial L/\partial \theta]$. Obtaining these gradients will enable optimization via gradient descent.

a. Gradient with respect to the initial state

The adjoint state is defined as $\mathbf{a}(t) = \partial L/\partial \mathbf{v}(t)$ and $\mathbf{a}(T)$ can be computed directly as long as L is differentiable while $\mathbf{a}(0)$ is the gradient that we want. By the chain rule,

$$\begin{aligned} a_i(t) &= \frac{\partial L}{\partial v_i(t)} = \sum_j \frac{\partial L}{\partial v_j(t+\epsilon)} \frac{\partial v_j(t+\epsilon)}{\partial v_i(t)} \\ &= \sum_j a_j(t+\epsilon) \frac{\partial \{v_j(t) + \epsilon f_j[\mathbf{v}(t), \boldsymbol{\theta}]\}}{\partial v_i(t)} \\ &= a_i(t+\epsilon) + \epsilon \sum_j a_j(t+\epsilon) \frac{\partial f_j[\mathbf{v}(t), \boldsymbol{\theta}]}{\partial v_i(t)}. \end{aligned} \quad (\text{A2})$$

Therefore, the adjoint state satisfies the differential equation:

$$\dot{a}_i(t) = \lim_{\epsilon \rightarrow 0} \frac{a_i(t+\epsilon) - a_i(t)}{\epsilon} = - \sum_j a_j(t) \frac{\partial f_j[\mathbf{v}(t), \boldsymbol{\theta}]}{\partial v_i(t)}. \quad (\text{A3})$$

More compactly,

$$\dot{\mathbf{a}}(t) = -C^T \mathbf{a}(t). \quad (\text{A4})$$

where \mathbf{a} is represented as a column vector and the matrix $C = \partial f[\mathbf{v}(t), \boldsymbol{\theta}]/\partial \mathbf{v}(t)$ is defined as $C_{ij} = \partial f_i[\mathbf{v}(t), \boldsymbol{\theta}]/\partial v_j(t)$. In other words, solving the above differential equation from $t = T$ to $t = 0$ allows us to obtain $\mathbf{a}(0) = \partial L/\partial \mathbf{v}(0)$.

b. Gradient with respect to ODE parameters

To compute the gradient $\partial L/\partial \theta$, we embed the parameters $\boldsymbol{\theta}$ into the state vector and consider a new ODE:

$$\frac{d}{dt} \begin{pmatrix} \mathbf{v} \\ \boldsymbol{\theta} \end{pmatrix} = \begin{pmatrix} f(\mathbf{v}, \boldsymbol{\theta}) \\ \mathbf{0} \end{pmatrix}. \quad (\text{A5})$$

This leads to a composite adjoint satisfying

$$\frac{d}{dt} \begin{pmatrix} \mathbf{a}(t) \\ \mathbf{a}_\theta(t) \end{pmatrix} = - \begin{pmatrix} \frac{\partial f[\mathbf{v}(t), \boldsymbol{\theta}]}{\partial \mathbf{v}(t)} & \frac{\partial f[\mathbf{v}(t), \boldsymbol{\theta}]}{\partial \boldsymbol{\theta}} \\ \mathbf{0} & \mathbf{0} \end{pmatrix}^T \begin{pmatrix} \mathbf{a}(t) \\ \mathbf{a}_\theta(t) \end{pmatrix}. \quad (\text{A6})$$

Define a matrix $D = \partial f[\mathbf{v}(t), \boldsymbol{\theta}]/\partial \boldsymbol{\theta}$ as $D_{ij} = \partial f_i[\mathbf{v}(t), \boldsymbol{\theta}]/\partial \theta_j$, then we have

$$\dot{\mathbf{a}}_\theta(t) = -D^T \mathbf{a}(t). \quad (\text{A7})$$

Notice that $\mathbf{a}_\theta(T) = 0$ since L does not explicitly depend on $\boldsymbol{\theta}$.

2. Adjoint method for the master equation

The above derivation works for general ODEs and here we would like to adapt the results to a specific type of ODE, the quantum master equation.

a. Gradient with respect to the initial state

It is easier to take derivatives with respect to the initial density matrix by working with superoperators. Consider the linear transformation $|i\rangle \langle j| \rightarrow |i\rangle \otimes |j\rangle$ that maps a density matrix $\rho = \sum \rho_{ij} |i\rangle \langle j|$ to a state vector $\bar{\rho} = \sum \rho_{ij} |i\rangle \otimes |j\rangle$. By definition it is straightforward to check the following relation for left and right multiplication of an operator:

$$A\rho B \rightarrow (A \otimes B^T)\bar{\rho}. \quad (\text{A8})$$

Therefore, the master equation, Eq. (1), is equivalent to

$$\begin{aligned} \dot{\bar{\rho}} &= -i(H \otimes I - I \otimes H^T)\bar{\rho} + \sum_{k=1}^K \beta_k \left(A_k \otimes A_k^* \right. \\ &\quad \left. - \frac{1}{2} A_k^\dagger A_k \otimes I - \frac{1}{2} I \otimes (A_k^\dagger A_k)^T \right) \bar{\rho} \\ &= M\bar{\rho}. \end{aligned} \quad (\text{A9})$$

To derive the adjoint equation in the presence of complex numbers, we could simply separate the real part (label x) and imaginary part (label y). The master equation can be written as

$$\begin{aligned} \frac{d}{dt} \begin{pmatrix} \bar{\rho}_x \\ \bar{\rho}_y \end{pmatrix} &= (M_x + iM_y)(\bar{\rho}_x + i\bar{\rho}_y) \\ &= \begin{pmatrix} M_x \bar{\rho}_x - M_y \bar{\rho}_y \\ M_x \bar{\rho}_y + M_y \bar{\rho}_x \end{pmatrix} = \begin{pmatrix} M_x & -M_y \\ M_y & M_x \end{pmatrix} \begin{pmatrix} \bar{\rho}_x \\ \bar{\rho}_y \end{pmatrix} \\ &= \mathbf{M} \begin{pmatrix} \bar{\rho}_x \\ \bar{\rho}_y \end{pmatrix}. \end{aligned} \quad (\text{A10})$$

Now we could calculate the C matrix by

$$C_{ij} = \frac{\partial [\mathbf{M}\rho(t)]_i}{\partial \rho_j(t)} = \frac{\partial \sum_k M_{ik} \rho_k(t)}{\partial \rho_j(t)} = M_{ij}, \quad (\text{A11})$$

which gives $C = \mathbf{M}$. Therefore, the adjoint equation is given by

$$\frac{d}{dt} \begin{pmatrix} \frac{\partial L}{\partial \bar{\rho}_x} \\ \frac{\partial L}{\partial \bar{\rho}_y} \end{pmatrix} = - \begin{pmatrix} M_x^T & M_y^T \\ -M_y^T & M_x^T \end{pmatrix} \begin{pmatrix} \frac{\partial L}{\partial \bar{\rho}_x} \\ \frac{\partial L}{\partial \bar{\rho}_y} \end{pmatrix}. \quad (\text{A12})$$

This could be simplified by introducing the complex adjoint

$$\bar{a} = \frac{\partial L}{\partial \bar{\rho}_x} + i \frac{\partial L}{\partial \bar{\rho}_y} = \sum a_{ij} |i\rangle \otimes |j\rangle, \quad a_{ij} = \frac{\partial L}{\partial \rho_{ij}^x} + i \frac{\partial L}{\partial \rho_{ij}^y} \quad (\text{A13})$$

such that

$$\dot{\bar{a}} = -(M_x^T - iM_y^T) \left(\frac{\partial L}{\partial \bar{\rho}_x} + i \frac{\partial L}{\partial \bar{\rho}_y} \right) = -M^\dagger \bar{a}. \quad (\text{A14})$$

More explicitly,

$$\begin{aligned} \dot{\bar{a}} &= -M^\dagger \bar{a} = -i(H \otimes I - I \otimes H^T) \bar{a} - \sum_{k=1}^K \beta_k \left(A_k^\dagger \otimes A_k^T \right. \\ &\quad \left. - \frac{1}{2} A_k^\dagger A_k \otimes I - \frac{1}{2} I \otimes (A_k^\dagger A_k)^T \right) \bar{a}. \end{aligned} \quad (\text{A15})$$

Now we inverse the mapping and define the adjoint matrix

$$\bar{a} = \sum a_{ij} |i\rangle \otimes |j\rangle \rightarrow a = \sum a_{ij} |i\rangle \langle j| \quad (\text{A16})$$

and the adjoint equation has a similar form as the original master equation:

$$\dot{a} = -i[H, a] - \sum_{k=1}^K \beta_k \left(A_k^\dagger a A_k - \frac{1}{2} \{A_k^\dagger A_k, a\} \right). \quad (\text{A17})$$

Starting from $a(T)$ and solving the adjoint equation backward in time to $t = 0$ gives $a(0)$, which is the gradient with respect to the initial density matrix.

b. Gradient with respect to system parameters

Going back to the superoperator representation, Eq. (A10), and taking derivative with respect to some ODE parameter θ :

$$\begin{aligned} \dot{a}_\theta(t) &= - \left[\partial_\theta \mathbf{M} \begin{pmatrix} \bar{\rho}_x \\ \bar{\rho}_y \end{pmatrix} \right]^T \begin{pmatrix} \frac{\partial L}{\partial \bar{\rho}_x} \\ \frac{\partial L}{\partial \bar{\rho}_y} \end{pmatrix} = -(\bar{\rho}_x^T, \bar{\rho}_y^T) \partial_\theta \mathbf{M}^T \begin{pmatrix} \frac{\partial L}{\partial \bar{\rho}_x} \\ \frac{\partial L}{\partial \bar{\rho}_y} \end{pmatrix} \\ &= -(\bar{\rho}_x^T, \bar{\rho}_y^T) \begin{pmatrix} \partial_\theta M_x^T & \partial_\theta M_y^T \\ -\partial_\theta M_y^T & \partial_\theta M_x^T \end{pmatrix} \begin{pmatrix} \frac{\partial L}{\partial \bar{\rho}_x} \\ \frac{\partial L}{\partial \bar{\rho}_y} \end{pmatrix} \\ &= -(\bar{\rho}_x^T \partial_\theta M_x^T - \bar{\rho}_y^T \partial_\theta M_y^T, \bar{\rho}_x^T \partial_\theta M_y^T + \bar{\rho}_y^T \partial_\theta M_x^T) \begin{pmatrix} \frac{\partial L}{\partial \bar{\rho}_x} \\ \frac{\partial L}{\partial \bar{\rho}_y} \end{pmatrix} \\ &= - \left[(\partial_\theta M \bar{\rho})_x^T \frac{\partial L}{\partial \bar{\rho}_x} + (\partial_\theta M \bar{\rho})_y^T \frac{\partial L}{\partial \bar{\rho}_y} \right]. \end{aligned} \quad (\text{A18})$$

Define

$$\bar{\Delta}_\theta = \partial_\theta M \bar{\rho} = \sum \Delta_{ij} |i\rangle \otimes |j\rangle \rightarrow \Delta_\theta = \sum \Delta_{ij} |i\rangle \langle j| \quad (\text{A19})$$

then the gradient could be simplified as

$$\dot{a}_\theta(t) = - \sum_{ij} (\Delta_{ij}^x a_{ij}^x + \Delta_{ij}^y a_{ij}^y) = -\text{ReTr} [\Delta_\theta a^\dagger(t)]. \quad (\text{A20})$$

From the master equation, it is not hard to see that

$$\begin{aligned} \Delta_{\alpha_j} &= -i[H_j, \rho(t)], \\ \Delta_{\beta_k} &= A_k \rho(t) A_k^\dagger - \frac{1}{2} \{A_k^\dagger A_k, \rho(t)\}. \end{aligned} \quad (\text{A21})$$

Therefore, after solving for $\rho(t)$ from Eq. (1) and $a(t)$ from Eq. (A17), we could solve $a_\theta(t)$ by integrating Eq. (A20) backward in time starting from $a_\theta(T) = 0$.

APPENDIX B: AVERAGE FIDELITY

We could evaluate the integration over Bloch sphere in the definition of average fidelity [main text Eq. (3)], which leads to a simpler expression to work with

$$\begin{aligned} \bar{F}(t) &= \text{Tr} \left[\left(\frac{1}{3} \hat{\rho}_{00} + \frac{1}{6} \hat{\rho}_{11} \right) \hat{\rho}_{00}(t) \right] \\ &\quad + \text{Tr} \left[\left(\frac{1}{6} \hat{\rho}_{00} + \frac{1}{3} \hat{\rho}_{11} \right) \hat{\rho}_{11}(t) \right] \\ &\quad + \text{Re} \left\{ \text{Tr} \left[\frac{1}{3} \hat{\rho}_{01} \hat{\rho}_{10}(t) \right] \right\}. \end{aligned} \quad (\text{B1})$$

Other fidelity definitions are also applicable as long as the gradients are computable. For example, we could learn AQEC with the entanglement fidelity [24]

$$\bar{F}(t) = \frac{1}{4} \text{Tr} [\hat{\rho}_{00} \hat{\rho}_{00}(t) + \hat{\rho}_{11} \hat{\rho}_{11}(t) + \hat{\rho}_{01} \hat{\rho}_{10}(t) + \hat{\rho}_{10} \hat{\rho}_{01}(t)]. \quad (\text{B2})$$

From our experience, we did not observe any substantial differences in terms of training speed and optimization results when using entanglement fidelity compared to the average fidelity.

1. Modified average fidelity

In practice, we find out that there is a simple modification of the average fidelity that helps avoiding certain local minima during the training. Instead of learning an identity map on the Bloch sphere, we could aim at preserving the Bloch sphere up to an arbitrary rotation in the logical subspace. This modification extends the set of Hamiltonians that protects a given QEC code, which could potentially accelerate the AutoQEC searching.

Analytically deriving the modified average fidelity turns out to be challenging for general rotations on the Bloch sphere. We therefore restrict the allowed rotations to only

along the Z axis:

$$\begin{aligned}\hat{U}|\psi_0\rangle &= |\psi_0\rangle, \\ \hat{U}|\psi_1\rangle &= e^{i\varphi}|\psi_1\rangle.\end{aligned}\quad (\text{B3})$$

The modified average fidelity becomes

$$\begin{aligned}\bar{F}(t) &= \max_{\hat{U}} \text{Tr} \left[\hat{U} \left(\frac{1}{3} \hat{\rho}_{00} + \frac{1}{6} \hat{\rho}_{11} \right) \hat{U}^\dagger \hat{\rho}_{00}(t) \right] \\ &+ \text{Tr} \left[\hat{U} \left(\frac{1}{6} \hat{\rho}_{00} + \frac{1}{3} \hat{\rho}_{11} \right) \hat{U}^\dagger \hat{\rho}_{11}(t) \right] \\ &+ \text{Re} \left\{ \text{Tr} \left[\frac{1}{3} \hat{U} \hat{\rho}_{01} \hat{U}^\dagger \hat{\rho}_{10}(t) \right] \right\} \\ &= \max_{\varphi} \text{Tr} \left[\left(\frac{1}{3} \hat{\rho}_{00} + \frac{1}{6} \hat{\rho}_{11} \right) \hat{\rho}_{00}(t) \right] \\ &+ \text{Tr} \left[\left(\frac{1}{6} \hat{\rho}_{00} + \frac{1}{3} \hat{\rho}_{11} \right) \hat{\rho}_{11}(t) \right] \\ &+ \text{Re} \left\{ \text{Tr} \left[\frac{1}{3} e^{-i\varphi} \hat{\rho}_{01} \hat{\rho}_{10}(t) \right] \right\} \\ &= \text{Tr} \left[\left(\frac{1}{3} \hat{\rho}_{00} + \frac{1}{6} \hat{\rho}_{11} \right) \hat{\rho}_{00}(t) \right] \\ &+ \text{Tr} \left[\left(\frac{1}{6} \hat{\rho}_{00} + \frac{1}{3} \hat{\rho}_{11} \right) \hat{\rho}_{11}(t) \right] \\ &+ \left| \text{Tr} \left[\frac{1}{3} \hat{\rho}_{01} \hat{\rho}_{10}(t) \right] \right|,\end{aligned}\quad (\text{B4})$$

where the only change compared to Eq. (B1) is to replace the real part of $\text{Tr}[\hat{\rho}_{01}\hat{\rho}_{10}(t)]$ with its absolute value. Throughout this paper, we use this modified average fidelity [Eq. (B4)] as the objective function for `AutoQEC`.

APPENDIX C: DERIVATION OF THE $\sqrt{3}$ CODE

With $d = 2$ Hamiltonian, `AutoQEC` discovered an error correcting code, which we were not able to find in the literature. This simple “ $\sqrt{3}$ ” code warrants further investigation, and here we derive it analytically based on the Hamiltonian distance constraints and QEC properties. Notice that the AQEC Hamiltonian for a given code is not unique—we therefore make some assumptions about the Hamiltonian structure to simplify the derivation.

1. General results

Consider the problem of correcting a single-photon-loss error with a bosonic mode. The logical states are $|\psi_0\rangle$ and $|\psi_1\rangle$. For simplicity, we assume the error states $|\psi_2\rangle \propto \hat{a}|\psi_0\rangle$ and $|\psi_3\rangle \propto \hat{a}|\psi_1\rangle$ are also mutually orthogonal to both logical states. Therefore, $\{|\psi_0\rangle, |\psi_1\rangle, |\psi_2\rangle, |\psi_3\rangle\}$ forms the basis for a four-dimensional subspace \mathcal{H}_1 . We choose the Hilbert space cutoff $|N\rangle$ as the highest Fock

level that has a nonzero overlap with either $|\psi_0\rangle$ or $|\psi_1\rangle$ (total Hilbert-space dimension $N + 1$). Now the Hilbert space is decomposed into \mathcal{H}_1 and its orthogonal complement \mathcal{H}_2 ($\mathcal{H} = \mathcal{H}_1 \oplus \mathcal{H}_2$) where a set of orthogonal basis for \mathcal{H}_2 is $\{|\psi_4\rangle, \dots, |\psi_N\rangle\}$.

To correct the single-photon-loss error autonomously, the Hamiltonian should include the following terms:

$$\hat{H} = (|\psi_0\rangle\langle\psi_2| + |\psi_1\rangle\langle\psi_3|) \otimes |e\rangle\langle g| + \text{h.c.}, \quad (\text{C1})$$

which basically maps the error states to the correct logical states and excited the qubit: $|\psi_2, g\rangle \leftrightarrow |\psi_0, e\rangle$, and $|\psi_3, g\rangle \leftrightarrow |\psi_1, e\rangle$. After relaxation of the ancilla qubit, the error states $|\psi_2\rangle$ and $|\psi_3\rangle$ are mapped back to the logical states $|\psi_0\rangle$ and $|\psi_1\rangle$ while maintaining the relative phase between them due to the identical Rabi rate in the Hamiltonian. Adiabatically eliminating the ancilla qubit results in an effective dissipator $D[|\psi_0\rangle\langle\psi_2| + |\psi_1\rangle\langle\psi_3|]$, which provides an alternative way of understanding the reduced dynamics for the bosonic mode.

The Hamiltonian, Eq. (C1), is conceptually simple, but may be difficult to generate in experiment since it can be highly nonlocal in the Fock basis. In the case of the smallest binomial code $|\psi_0\rangle = 1/\sqrt{2}(|0\rangle + |4\rangle)$ and $|\psi_1\rangle = |2\rangle$, realizing Eq. (C1) would require a coupling term $|3, g\rangle\langle 0, e|$, which does not occur naturally [3,9]. Going to a higher-order binomial code is even worse since it requires even more nonlocal interaction between Fock states.

This is where states in the orthogonal subspace \mathcal{H}_2 could contribute. The basic idea is that those states would not change the QEC behavior, but their proper combinations could cancel certain nonlocal interactions in Eq. (C1) and make the total Hamiltonian easier to implement. For this purpose, the general form of the QEC Hamiltonian is (we ignore all $|g\rangle\langle g|$ and $|e\rangle\langle e|$ terms since those would not solve the locality problem anyway)

$$\begin{aligned}\hat{H} &= \tilde{H}^\dagger \otimes |e\rangle\langle g| + \tilde{H} \otimes |g\rangle\langle e|, \\ \tilde{H} &= |\psi_2\rangle\langle\psi_0| + |\psi_3\rangle\langle\psi_1| + \sum_{ij}^N \beta_{ij} |\psi_i\rangle\langle\psi_j|.\end{aligned}\quad (\text{C2})$$

We impose a number of constraints on the coefficients β_{ij} such that the summation part of \tilde{H} does not modify the error correction dynamics. In particular, we require that $\beta_{ij} = 0$ for $i < 4$ and $j < 2$. The requirement $j < 2$ removes overlap with the states $|\psi_{0\sim 1}, e\rangle$ —we want only the first part of \tilde{H} to perform this correction function. Similarly, removing $i < 4$ prevents overlap with states $|\psi_{0\sim 3}, g\rangle$, which is important for preventing the summation part of the Hamiltonian from causing states to transition into the code and error subspaces.

Having set these conditions on \tilde{H} , we now quantify the notion of locality for the Hamiltonian. We

define the distance of a Hamiltonian H to be d if $\tilde{H}_{mn} \equiv \langle m | \tilde{H} | n \rangle = 0, \forall |m - n| > d, 0 \leq m, n \leq N$. From our numerical search (Fig. 2), we found that $d = 1$ Hamiltonians generate only trivial error correcting codes. Therefore, we consider the $d = 2$ case, which seems to be the minimal distance required for QEC exceeding break even. More explicitly, a $d = 2$ Hamiltonian satisfies

$$\begin{pmatrix} 0 & \tilde{H}_{03} & \tilde{H}_{04} & \cdots & \tilde{H}_{0N} \\ \tilde{H}_{30} & 0 & \tilde{H}_{14} & \cdots & \tilde{H}_{1N} \\ \tilde{H}_{40} & \tilde{H}_{41} & 0 & \cdots & \tilde{H}_{2N} \\ \vdots & & & & \\ \tilde{H}_{N0} & \tilde{H}_{N1} & \cdots & \tilde{H}_{N,N-3} & 0 \end{pmatrix} = \mathbf{0}. \quad (\text{C3})$$

The goal here is to find \tilde{H} , in other words, we solve for the coefficients β_{ij} as well as the logical states while satisfying these locality constraints.

2. Example of the $\sqrt{3}$ code

We demonstrate how to solve this problem with a concrete example. Numerically the $\sqrt{3}$ code we found with the $d = 2$ Hamiltonian had logical states of the form

$$\begin{aligned} |\psi_0\rangle &= a_0 |0\rangle + a_3 |3\rangle, \\ |\psi_1\rangle &= a_1 |1\rangle + a_4 |4\rangle + a_6 |6\rangle. \end{aligned} \quad (\text{C4})$$

Since the two logical states do not share any Fock basis, we can always make all coefficients a_0, a_3, a_1, a_4, a_6 real by doing the basis transformation $|n\rangle \rightarrow e^{i\theta_n} |n\rangle$. The error states are

$$\begin{aligned} |\psi_2\rangle &= |2\rangle \propto \hat{a} |\psi_0\rangle, \\ |\psi_3\rangle &= \mathcal{N}_1 (a_1 |0\rangle + 2a_4 |3\rangle + \sqrt{6}a_6 |5\rangle) \propto \hat{a} |\psi_1\rangle. \end{aligned} \quad (\text{C5})$$

Notice that if Eq. (C3) does have a solution, the solution always exists no matter how we choose the basis for the orthogonal subspace \mathcal{H}_2 . In other words, we could always represent the new basis as linear combinations of the old basis and that together with the old solution β_{ij} gives the new solution β'_{ij} . Therefore, here we have complete freedom to select the basis $\{|\psi_4\rangle, |\psi_5\rangle, |\psi_6\rangle\}$ for \mathcal{H}_2 and for convenience of further analysis we make the following choice [notation $\psi_i(n) = \langle n | \psi_i \rangle$]:

$$\begin{aligned} |\psi_4\rangle &= \psi_4(1) |1\rangle + \psi_4(4) |4\rangle + \psi_4(6) |6\rangle, \\ |\psi_5\rangle &= \psi_5(1) |1\rangle + \psi_5(4) |4\rangle + \psi_5(6) |6\rangle, \\ |\psi_6\rangle &= \psi_6(0) |0\rangle + \psi_6(3) |3\rangle + \psi_6(5) |5\rangle. \end{aligned} \quad (\text{C6})$$

We can make all $\psi_i(n)$ to be real here, which leads to all β_{ij} also being real. With this basis choice, many constraints in Eq. (C3) can be easily satisfied either automatically or by setting certain $\beta_{ij} = 0$. More specifically, for any $|m -$

$n| > 2$ such that $\langle m | (|\psi_2\rangle \langle \psi_0| + |\psi_3\rangle \langle \psi_1|) | n \rangle = 0$, there are two different cases:

1. $\langle m | (|\psi_i\rangle \langle \psi_j|) | n \rangle = 0, \forall i, j$: in this case $\tilde{H}_{mn} = 0$ is already satisfied;
2. there exists i, j such that $\langle m | (|\psi_i\rangle \langle \psi_j|) | n \rangle \neq 0$: in this case we just set $\beta_{ij} = 0$.

Therefore, the only nontrivial constraints from Eq. (C3) are those with $\langle m | (|\psi_2\rangle \langle \psi_0| + |\psi_3\rangle \langle \psi_1|) | n \rangle \neq 0$, which are $\tilde{H}_{04}, \tilde{H}_{06}, \tilde{H}_{36}, \tilde{H}_{51}$. It is easy to see that the only terms in Eq. (C2) that will contribute to these matrix elements are $|\psi_6\rangle \langle \psi_4|$ and $|\psi_6\rangle \langle \psi_5|$. With these analyses, the ansatz Hamiltonian, Eq. (C2), can greatly simplify to the following:

$$\tilde{H} = |\psi_2\rangle \langle \psi_0| + |\psi_3\rangle \langle \psi_1| + \beta_1 |\psi_6\rangle \langle \psi_4| + \beta_2 |\psi_6\rangle \langle \psi_5|, \quad (\text{C7})$$

where the two free parameters β_1 and β_2 satisfy a set of linear equations

$$\tilde{H}_{04} = \psi_3(0)\psi_1(4) + \beta_1\psi_6(0)\psi_4(4) + \beta_2\psi_6(0)\psi_5(4) = 0, \quad (\text{C8a})$$

$$\tilde{H}_{06} = \psi_3(0)\psi_1(6) + \beta_1\psi_6(0)\psi_4(6) + \beta_2\psi_6(0)\psi_5(6) = 0, \quad (\text{C8b})$$

$$\tilde{H}_{36} = \psi_3(3)\psi_1(6) + \beta_1\psi_6(3)\psi_4(6) + \beta_2\psi_6(3)\psi_5(6) = 0, \quad (\text{C8c})$$

$$\tilde{H}_{51} = \psi_3(5)\psi_1(1) + \beta_1\psi_6(5)\psi_4(1) + \beta_2\psi_6(5)\psi_5(1) = 0. \quad (\text{C8d})$$

The crucial observation here is that the number of equations, four, is larger than the number of parameters, two, which means the coefficients must be linearly dependent. Since these coefficients are essentially functions of $|\psi_0\rangle$ and $|\psi_1\rangle$, this eventually provides the extra constraints for determining the logical states. Here there should be $4 - 2 = 2$ constraints in total.

Below we show in details how to obtain the two constraints and eventually the two logical states. Comparing Eqs. (C8b) and (C8c), it is easy to see that the first constraint is

$$\frac{\psi_3(0)}{\psi_3(3)} = \frac{\psi_6(0)}{\psi_6(3)}. \quad (\text{C9})$$

To get the second constraint, let us multiply Eq. (C8a) with $\psi_1(4)$, multiply Eq. (C8b) with $\psi_1(6)$, and then add them together:

$$\begin{aligned} &\psi_3(0) \{ [\psi_1(4)]^2 + [\psi_1(6)]^2 \} \\ &+ \beta_1 \psi_6(0) [\psi_4(4)\psi_1(4) + \psi_4(6)\psi_1(6)] \\ &+ \beta_2 \psi_6(0) [\psi_5(4)\psi_1(4) + \psi_5(6)\psi_1(6)] = 0. \end{aligned} \quad (\text{C10})$$

Using the fact that $|\psi_1\rangle$ is normalized and orthogonal to both $|\psi_4\rangle$ and $|\psi_5\rangle$, we have

$$\begin{aligned} \psi_3(0)\{1 - [\psi_1(1)]^2\} + \beta_1\psi_6(0)[- \psi_4(1)\psi_1(1)] \\ + \beta_2\psi_6(0)[- \psi_5(1)\psi_1(1)] &= 0 \\ \Rightarrow -\psi_3(0)\frac{1 - [\psi_1(1)]^2}{\psi_1(1)} + \beta_1\psi_6(0)\psi_4(1) \\ + \beta_2\psi_6(0)\psi_5(1) &= 0. \end{aligned} \quad (\text{C11})$$

Compare this with Eq. (C8d), we immediately obtain the second constraint:

$$\begin{aligned} -\psi_3(0)\frac{1 - [\psi_1(1)]^2}{\psi_1(1)\psi_6(0)} = \frac{\psi_3(5)\psi_1(1)}{\psi_6(5)} \\ \Rightarrow \psi_3(0)\psi_6(5)\{1 - [\psi_1(1)]^2\} \\ + \psi_3(5)\psi_6(0)[\psi_1(1)]^2 = 0. \end{aligned} \quad (\text{C12})$$

Let us explicitly list all the relevant states here

$$\begin{aligned} |\psi_0\rangle &= a_0 |0\rangle + a_3 |3\rangle, \\ |\psi_1\rangle &= a_1 |1\rangle + a_4 |4\rangle + a_6 |6\rangle, \\ |\psi_3\rangle &= \mathcal{N}_1(a_1 |0\rangle + 2a_4 |3\rangle + \sqrt{6}a_6 |5\rangle), \\ |\psi_6\rangle &= \mathcal{N}_2(a_1 |0\rangle + 2a_4 |3\rangle + \beta |5\rangle), \end{aligned} \quad (\text{C13})$$

where we apply Eq. (C9) for $|\psi_6\rangle$ and β is another parameter. Combining the QEC criteria and Eq. (C12), we have

$$\begin{aligned} a_0^2 + a_3^2 &= 1, \\ a_1^2 + a_4^2 + a_6^2 &= 1, \\ a_0a_1 + 2a_3a_4 &= 0, \\ 3a_3^2 &= a_1^2 + 4a_4^2 + 6a_6^2, \\ a_1^2 + 4a_4^2 + \sqrt{6}\beta a_6 &= 0, \\ \beta(1 - a_1^2) + \sqrt{6}a_6a_1^2 &= 0. \end{aligned} \quad (\text{C14})$$

We have six equations and six parameters in total, and the solution is (there is some freedom to choose the signs, which again is just a trivial basis transformation)

$$\begin{aligned} a_0 = \sqrt{1 - \frac{1}{\sqrt{3}}}, a_3 = \frac{1}{\sqrt[4]{3}}, a_1 = \sqrt{\frac{2(6 - \sqrt{3})}{\sqrt{3} + 9}}, \\ a_4 = -\sqrt{\frac{(\sqrt{3} - 1)(6 - \sqrt{3})}{2(\sqrt{3} + 9)}}, a_6 = \sqrt{\frac{3 - \sqrt{3}}{2(\sqrt{3} + 9)}}. \end{aligned} \quad (\text{C15})$$

Therefore, the logical states of the $\sqrt{3}$ code are

$$\begin{aligned} |\psi_0\rangle &= \sqrt{1 - \frac{1}{\sqrt{3}}} |0\rangle + \frac{1}{\sqrt[4]{3}} |3\rangle, \\ |\psi_1\rangle &= \sqrt{\frac{2(6 - \sqrt{3})}{\sqrt{3} + 9}} |1\rangle - \sqrt{\frac{(\sqrt{3} - 1)(6 - \sqrt{3})}{2(\sqrt{3} + 9)}} |4\rangle \\ &\quad + \sqrt{\frac{3 - \sqrt{3}}{2(\sqrt{3} + 9)}} |6\rangle. \end{aligned} \quad (\text{C16})$$

Notice that the average number of photons in the code-words is $3|a_3|^2 = \sqrt{3}$.

Now we could complete all basis states and the Hamiltonian, Eq. (C7). The basis of \mathcal{H}_2 ,

$$\begin{aligned} |\psi_6\rangle &= \mathcal{N}_2(a_1 |0\rangle + 2a_4 |3\rangle + \beta |5\rangle), \quad \beta = -\frac{a_1^2 + 4a_4^2}{\sqrt{6}a_6}, \\ |\psi_4\rangle &= \mathcal{N}_3(a_4 |1\rangle - a_1 |4\rangle), \\ |\psi_5\rangle &= \mathcal{N}_4(a_1 |1\rangle + a_4 |4\rangle + \beta' |6\rangle), \quad \beta' = -\frac{a_1^2 + a_4^2}{a_6} \end{aligned} \quad (\text{C17})$$

and the Hamiltonian parameters,

$$\beta_2 = -\frac{\mathcal{N}_1 a_6}{\mathcal{N}_2 \mathcal{N}_4 \beta'}, \quad \beta_1 = \frac{\mathcal{N}_1 a_4 (1 - a_6 / \beta')}{\mathcal{N}_2 \mathcal{N}_3 a_1}. \quad (\text{C18})$$

There are some extra complexities in constructing the AQEC Hamiltonian and we actually need to keep more terms from the summation in Eq. (C2) rather than just the β_1 and β_2 terms in Eq. (C7). To understand why this is required, let us study a simpler problem of stabilizing $|\psi\rangle = 1/\sqrt{2}(|0\rangle + |2\rangle)$ under photon-loss error. Even though the Hamiltonian $\hat{H} = (|0, e\rangle + |2, e\rangle)\langle 1, g| + \text{h.c.}$ corrects the error after a single-photon loss, it does not actually lead to state stabilization. The reason is that when no photon loss happens, the state evolves within the subspace $\{|0\rangle, |2\rangle\}$ under the non-Hermitian Hamiltonian $\hat{H}' = -i\kappa\hat{a}^\dagger\hat{a}/2$ and eventually becomes $|0\rangle$. This is because nondetection of a photon still provides us information about the state causing us to update it in a way that skews towards a lower number of photons. State stabilization must undo this effect. We protect $|\psi\rangle$ against \hat{H}' by engineering a large detuning for $|\psi\rangle$ within the subspace $\{|0\rangle, |2\rangle\}$. For example, adding extra terms such as $\Omega|\psi\rangle\langle\psi|$ or $\Omega|0\rangle\langle 2| + \text{h.c.}$ to \hat{H} will stabilize $|\psi\rangle$. This new interaction can be seen as rapidly repopulating the $|2\rangle$ component of the wavevector as it decays through nondetection of photons.

Similarly, Eq. (C7) protects only the logical states against single-photon-loss error, but not the nonunitary dynamics under \hat{H}' . Fortunately, keeping a few extra terms

from the summation in Eq. (C2) is sufficient to generate the large detuning without changing the Hamiltonian distance as well as the above derivation. The choices are not unique and one option is to add $|\psi_4\rangle\langle\psi_2|$ as well as $(a_6|4\rangle - a_4|6\rangle)\langle 5|$ in \tilde{H} , which produces similar results compared to the discovered code in Fig. 2(c)i. On the other hand, all these complications in constructing a proper AQEC Hamiltonian are automatically taken care of by AutoQEC through numerical optimization of the average fidelity.

APPENDIX D: MINIMIZING THE EMISSION BANDWIDTH \mathcal{B}

Here we prove the claim in the main text that for a harmonic oscillator coupled to a three-level qubit with Hamiltonian \hat{H}_{ab} in Eq. (7), the emission bandwidth \mathcal{B} is minimized when $g_1^2/\Delta_1 \approx g_2^2/\Delta_2$.

Proof. The Hamiltonian can be written in the subspace of $\{|n+2, g\rangle, |n+1, e\rangle, |n, f\rangle\}$ as a matrix

$$\begin{pmatrix} 0 & \sqrt{n+2}g_1 & 0 \\ \sqrt{n+2}g_1 & \Delta_1 & \sqrt{n+1}g_2 \\ 0 & \sqrt{n+1}g_2 & \Delta_2 \end{pmatrix} \quad (\text{D1})$$

and the eigenvalues satisfy

$$\lambda^3 - (\Delta_1 + \Delta_2)\lambda^2 + [\Delta_1\Delta_2 - (n+2)g_1^2 - (n+1)g_2^2]\lambda + (n+2)g_1^2\Delta_2 = 0. \quad (\text{D2})$$

In the dispersive regime $\Delta_{1,2} \gg g_{1,2}$, the eigenvalues can be expanded perturbatively as

$$\begin{aligned} \lambda &= \lambda_0 + \lambda_1 + \lambda_2 + \mathcal{O}\left(\frac{g^3}{\Delta^3}\right)g, \\ \lambda_1 &= \mathcal{O}\left(\frac{g}{\Delta}\right)g, \quad \lambda_2 = \mathcal{O}\left(\frac{g^2}{\Delta^2}\right)g. \end{aligned} \quad (\text{D3})$$

For dressed eigenstates $|\widetilde{n+2, g}\rangle$, $\lambda_0 = 0$ and

$$\begin{aligned} [\Delta_1\Delta_2 - (n+2)g_1^2 - (n+1)g_2^2]\lambda_1 + (n+2)g_1^2\Delta_2 &= 0 \\ \Rightarrow \lambda_1 &= -\frac{(n+2)g_1^2}{\Delta_1}, \end{aligned} \quad (\text{D4})$$

which agrees with the dispersive coupling Hamiltonian and no level nonlinearity shows up at this order. To the next

order,

$$\begin{aligned} [\Delta_1\Delta_2 - (n+2)g_1^2 - (n+1)g_2^2](\lambda_1 + \lambda_2) \\ - (\Delta_1 + \Delta_2)\lambda_1^2 + (n+2)g_1^2\Delta_2 &= 0, \end{aligned} \quad (\text{D5})$$

which gives

$$\lambda_2 = \frac{(n+2)g_1^2}{\Delta_1^2} \left[(n+2)\frac{g_1^2}{\Delta_1} - (n+1)\frac{g_2^2}{\Delta_2} \right]. \quad (\text{D6})$$

Notice that in general λ_2 will induce nonlinearity for the dressed states $|\widetilde{n, g}\rangle$ since it depends on n^2 . However, when $g_1^2/\Delta_1 = g_2^2/\Delta_2$ the dependence on n^2 is completely removed, which means the nonlinearity and therefore also the emission bandwidth \mathcal{B} is eliminated at this order. ■

1. Qubit choice for \hat{b}

The relevant dispersive coupling to the e levels is

$$\chi_e = \frac{2g_1^2}{\Delta_1} - \frac{g_2^2}{\Delta_2 - \Delta_1} \quad (\text{D7})$$

and at the minimal nonlinearity point, we have

$$\chi_e = \frac{g_1^2}{\Delta_1} \frac{r-2}{r-1}, \quad (\text{D8})$$

where $r = g_2^2/g_1^2 = \Delta_2/\Delta_1$. Ideally, χ_e should be as large as possible at this minimal nonlinearity point, such that we can selectively drive certain level transitions without introducing large \mathcal{B} . For a transmon qubit $r \approx 2 \Rightarrow \chi_e \approx 0$ and therefore cannot be used as qubit \hat{b} . Fortunately, other qubit designs could provide much more flexibility in engineering the coupling ratio r and $r \approx 1$ is favorable in terms of larger χ_e .

In this work, we choose a fluxonium type of Hamiltonian

$$\hat{H} = 4E_C\hat{n}^2 - E_J \cos(\hat{\phi} - \phi_{\text{ext}}) + \frac{1}{2}E_L\hat{\phi}^2 \quad (\text{D9})$$

for qubit \hat{b} . With realistic parameters $\phi_{\text{ext}} = 0$, $E_C/2\pi = 0.95$ GHz, $E_J/2\pi = 4.75$ GHz, and $E_L/2\pi = 0.65$ GHz, the coupling ratio is $r = g_2^2/g_1^2 = |\langle f|\hat{n}|\hat{e}\rangle|^2/|\langle e|\hat{n}|\hat{g}\rangle|^2 \approx 1.2$ with $\omega_{ge}/2\pi \approx 5.43$ GHz and $\omega_{ef}/2\pi \approx 3.87$ GHz.

APPENDIX E: FULL CIRCUIT DESIGN

In this section, we provide details for the full circuit simulation in Fig. 4(e). The AQEC Hamiltonian Eq. (6) can be

implemented with a more physical Hamiltonian

$$\hat{H} = \hat{H}_{ab} + [f_1(t)\hat{a}^\dagger + f_2(t)\hat{a} + f_3(t)\hat{a}^2] \hat{b}^\dagger + f_4(t)\hat{b}^\dagger \hat{c} + \text{h.c.}, \quad (\text{E1})$$

where

$$\begin{aligned} f_1(t) &= \sum_n \frac{\alpha_n^{(1)} e^{-i(E_{n,e} - E_{n-1,g})t}}{\langle \widetilde{n}, e | \hat{a}^\dagger \hat{b}^\dagger | \widetilde{n-1}, g \rangle}, \\ f_2(t) &= \sum_n \frac{\alpha_n^{(2)} e^{-i(E_{n,e} - E_{n+1,g})t}}{\langle \widetilde{n}, e | \hat{a} \hat{b}^\dagger | \widetilde{n+1}, g \rangle}, \\ f_3(t) &= \sum_n \frac{\alpha_n^{(3)} e^{-i(E_{n,e} - E_{n+2,g})t}}{\langle \widetilde{n}, e | \hat{a}^2 \hat{b}^\dagger | \widetilde{n+2}, g \rangle}, \\ f_4(t) &= \Omega \sum_n \frac{e^{-i(E_{n,e} - E_{n,g})t}}{\langle \widetilde{n}, e | \hat{b}^\dagger | \widetilde{n}, g \rangle}, \end{aligned} \quad (\text{E2})$$

and $|\widetilde{n}, g(e)\rangle$ are the dressed eigenstates of \hat{H}_{ab} with energies $E_{n,g(e)}$, i.e., $\hat{H}_{ab} = \sum_n E_{n,g} |\widetilde{n}, g\rangle \langle \widetilde{n}, g| + E_{n,e} |\widetilde{n}, e\rangle \langle \widetilde{n}, e|$ (we ignore $|\widetilde{n}, f\rangle$ here for notation simplicity). Now the dressed states $|\widetilde{n}, g\rangle$ replace the bare Fock states $|n, g\rangle$ in our definition of the logical basis in Eq. (C16) since the logical subspace should be preserved (up to a trivial phase accumulation) under the static Hamiltonian \hat{H}_{ab} without any drivings and dissipation. The required AQEC Hamiltonian, Eq. (6), should also translate accordingly into the dressed version to protect the logical subspace. For example, the type 1 coupling now becomes

$$\begin{aligned} \hat{H}^{(1)} &= \sum_n \alpha_n^{(1)} |n\rangle \langle n-1| \otimes \hat{b}^\dagger + \text{h.c.} \\ \rightarrow \hat{H}^{(1)} &= \sum_n \alpha_n^{(1)} |\widetilde{n}, e\rangle \langle \widetilde{n-1}, g| + \text{h.c.} \end{aligned} \quad (\text{E3})$$

Since \hat{H}_{ab} is in the dispersive regime, the dressed eigenstates are close to the bare Fock states and matrix elements such as $\langle \widetilde{n}, e | \hat{a}^\dagger \hat{b}^\dagger | \widetilde{n-1}, g \rangle$ will be close but not equal to \sqrt{n} .

To prove the equivalence between Eqs. (E1) and (6), we could derive the type 1 Hamiltonian step by step from the $f_1(t)\hat{a}^\dagger \hat{b}^\dagger$ term in Eq. (E1), and the type 2 and 3 Hamiltonians follow similar derivations. The operator $\hat{a}^\dagger \hat{b}^\dagger$ can be expanded explicitly in the dressed basis as

$$\hat{a}^\dagger \hat{b}^\dagger = \sum_{\substack{m, m' \\ s, s'}} \langle \widetilde{m}, s | \hat{a}^\dagger \hat{b}^\dagger | \widetilde{m}', s' \rangle |\widetilde{m}, s\rangle \langle \widetilde{m}', s'|, \quad (\text{E4})$$

where $m, m' = 0, 1, 2, \dots$ are the Fock indices and $s, s' = g, e, \dots$ are states of the qubit \hat{b} . Now $f_1(t)\hat{a}^\dagger \hat{b}^\dagger$ in the

rotating frame of \hat{H}_{ab} is given by

$$\begin{aligned} f_1(t)\hat{a}^\dagger \hat{b}^\dagger &= \sum_n \frac{\alpha_n^{(1)} e^{-i(E_{n,e} - E_{n-1,g})t}}{\langle \widetilde{n}, e | \hat{a}^\dagger \hat{b}^\dagger | \widetilde{n-1}, g \rangle} \\ &\times \sum_{\substack{m, m' \\ s, s'}} \langle \widetilde{m}, s | \hat{a}^\dagger \hat{b}^\dagger | \widetilde{m}', s' \rangle |\widetilde{m}, s\rangle \langle \widetilde{m}', s'| e^{i(E_{m,s} - E_{m',s'})t}. \end{aligned} \quad (\text{E5})$$

There are many terms in the summation and when $(m, s) = (n, e)$ and $(m', s') = (n-1, g)$ the term is time independent. The sum of all these static terms gives $\sum_n \alpha_n^{(1)} |\widetilde{n}, e\rangle \langle \widetilde{n-1}, g|$, which is exactly the desired type 1 coupling Hamiltonian. All other terms in the summation are time dependent and the minimal rotation rate of those terms is roughly the dispersive coupling strength $\chi \sim g_1^2/\Delta_1$ between \hat{a} and \hat{b} . Since we are operating in the regime of $\chi \gg |\alpha_n|$, the time-dependent terms can be dropped by the rotating wave approximation.

The relevant dissipators are $\{D[\sqrt{\kappa}\hat{a}], D[\sqrt{\kappa_q}\hat{c}]\}$, but to be more realistic we also include an extra dissipator $D[\sqrt{\kappa}\hat{b}]$ in the simulation. The coupling strength Ω between \hat{b} and \hat{c} is chosen such that the effective decay rate for \hat{b} after adiabatically eliminating \hat{c} [27] is still $4\Omega^2/\kappa_q = 2\pi \times 20$ kHz, the same as the value used in the numerical optimization. We set the decay rate of \hat{c} as $\kappa_q/2\pi = 100$ kHz.

The Hamiltonian, Eq. (E1), can be furthermore implemented with a circuit model

$$\begin{aligned} \hat{H} &= \omega_a \hat{a}^\dagger \hat{a} + \omega_{ge} |e\rangle \langle e| + (\omega_{ge} + \omega_{ef}) |f\rangle \langle f| + \omega_c \hat{c}^\dagger \hat{c} \\ &+ g_1 (\hat{a}^\dagger |g\rangle \langle e| + \hat{a} |e\rangle \langle g|) + g_2 (\hat{a} |f\rangle \langle e| + \hat{a}^\dagger |e\rangle \langle f|) \\ &+ \varepsilon_1(t) [g_{ab}^{(1)} \cos \hat{\phi}_{ab} + g_{bc}^{(1)} \cos \hat{\phi}_{bc}] \\ &+ \varepsilon_2(t) [g_{ab}^{(2)} \sin \hat{\phi}_{ab} + g_{bc}^{(2)} \sin \hat{\phi}_{bc}], \end{aligned} \quad (\text{E6})$$

where $\hat{\phi}_{xy} = \varphi_x(\hat{x} + \hat{x}^\dagger) + \varphi_y(\hat{y} + \hat{y}^\dagger)$ and the drivings are given by

$$\begin{aligned} \varepsilon_1(t) &= -2\text{Re} \left\{ \frac{1}{\varphi_a \varphi_b g_{ab}^{(1)}} [e^{-2i\omega_a t} f_1(t) + f_2(t)] \right. \\ &\quad \left. + \frac{1}{\varphi_b \varphi_c g_{bc}^{(1)}} e^{i(\omega_c - \omega_a)t} f_4(t) \right\} \\ \varepsilon_2(t) &= -2\text{Re} \left\{ \frac{2}{\varphi_a^2 \varphi_b g_{ab}^{(2)}} e^{i\omega_a t} f_3(t) \right\}, \end{aligned} \quad (\text{E7})$$

which are generated by the two independent flux pump through the larger and smaller loops [7] in Fig. 4(c).

To derive Eq. (E1) from Eq. (E6), we could go into the rotating frame of $\omega_a(\hat{a}^\dagger\hat{a} + \hat{b}^\dagger\hat{b}) + \omega_c\hat{c}^\dagger\hat{c}$ where the static part of Eq. (E6) becomes exactly \hat{H}_{ab} with $\Delta_1 = \omega_{ge} - \omega_a$ and $\Delta_2 = \Delta_1 + \omega_{ef} - \omega_a$, and the flux driving part of Eq. (E6) becomes

$$\begin{aligned} & \varepsilon_1(t) \left[g_{ab}^{(1)} \cos \hat{\phi}_{ab}(t) + g_{bc}^{(1)} \cos \hat{\phi}_{bc}(t) \right] \\ & + \varepsilon_2(t) \left[g_{ab}^{(2)} \sin \hat{\phi}_{ab}(t) + g_{bc}^{(2)} \sin \hat{\phi}_{bc}(t) \right], \end{aligned} \quad (\text{E8})$$

where

$$\begin{aligned} \hat{\phi}_{ab}(t) &= \varphi_a(\hat{a}e^{-i\omega_a t} + \hat{a}^\dagger e^{i\omega_a t}) + \varphi_b(\hat{b}e^{-i\omega_a t} + \hat{b}^\dagger e^{i\omega_a t}), \\ \hat{\phi}_{bc}(t) &= \varphi_b(\hat{b}e^{-i\omega_a t} + \hat{b}^\dagger e^{i\omega_a t}) + \varphi_c(\hat{c}e^{-i\omega_c t} + \hat{c}^\dagger e^{i\omega_c t}). \end{aligned} \quad (\text{E9})$$

Superconducting circuits usually satisfy $\varphi_a, \varphi_b, \varphi_c \ll 1$ and therefore we could Taylor expand the cos and sin interaction and keep only the lower-order terms. As an example, we derive the $f_3(t)\hat{a}^2\hat{b}^\dagger$ term [33] in Eq. (E1) from $\varepsilon_2(t)g_{ab}^{(2)} \sin \hat{\phi}_{ab}(t)$. Keeping up to the third order

$$\varepsilon_2(t)g_{ab}^{(2)} \sin \hat{\phi}_{ab}(t) \approx \varepsilon_2(t)g_{ab}^{(2)} \left[\hat{\phi}_{ab}(t) - \frac{\hat{\phi}_{ab}^3(t)}{6} \right]. \quad (\text{E10})$$

Now we would like to calculate the frequency for each term in the expansion and drop the fast rotating ones. From the expression of \hat{H}_{ab} we can estimate that $f_i(t) \sim e^{-i\Delta_i t}$, $i = 1, 2, 3, 4$ in the dispersive regime, and in the rotating frame of \hat{H}_{ab} we have $\hat{b} \sim e^{-i\Delta_1 t}$. Therefore, the $\hat{a}, \hat{a}^\dagger, \hat{b}, \hat{b}^\dagger$ terms in $\varepsilon_2(t)g_{ab}^{(2)}\hat{\phi}_{ab}(t)$ are oscillating at frequencies $-\Delta_1, 2\omega_a - \Delta_1, -2\Delta_1, 2\omega_a$, respectively, and can all be dropped with proper frequency placement. For all terms in the expansion of $\hat{\phi}_{ab}^3(t)$, it is straightforward to see that there is only one slow term

$$\begin{aligned} & \varepsilon_2(t)g_{ab}^{(2)} \left(-\frac{1}{6} \right) \left(3\varphi_a^2\varphi_b\hat{a}^2\hat{b}^\dagger e^{-i\omega_a t} \right) \\ & = 2\text{Re} \left\{ f_3(t)\hat{a}^2\hat{b}^\dagger \right\} = f_3(t)\hat{a}^2\hat{b}^\dagger + \text{h.c.}, \end{aligned} \quad (\text{E11})$$

which is what we want to engineer, and all other fast oscillating terms can be dropped. Similarly, by expanding $\cos \hat{\phi} \approx 1 - \hat{\phi}^2/2$ and checking the frequencies for all the terms in $-\varepsilon_1(t)g_{ab}^{(1)}\hat{\phi}_{ab}^2(t)/2$ and $-\varepsilon_1(t)g_{bc}^{(1)}\hat{\phi}_{bc}^2(t)/2$, we could show that the slow oscillating terms from Eq. (E6) exactly reduces to Eq. (E1).

To ensure the validity of rotating wave approximation, we place the frequencies at $\omega_a/2\pi = 3.5$ GHz and $\omega_c/2\pi = 2.5$ GHz with qubit \hat{b} frequencies from the previous section. We also choose $\varphi_a = \varphi_b = \varphi_c = 0.1$ such that higher-order terms in the cos and sin expansions can

be safely dropped. All AQEC Hamiltonian parameters as well as the logical basis states are directly imported from the AutoQEC optimization result instead of using the analytical results in Appendix C. We use QuTiP [34,35] for the full circuit simulation.

APPENDIX F: ADDITIONAL COMMENTS ON THE OPTIMIZATION RESULTS

1. Exceed break even with partial protection

We further investigate the result in Fig. 2(c)ii, which represents a class of optimization results that perform better than break-even fidelity but worse than full QEC codes. Figure 5(a) shows the Wigner functions for the code subspace as well as both logical states, and Fig. 5(b) shows the photon-number distribution for the logical states

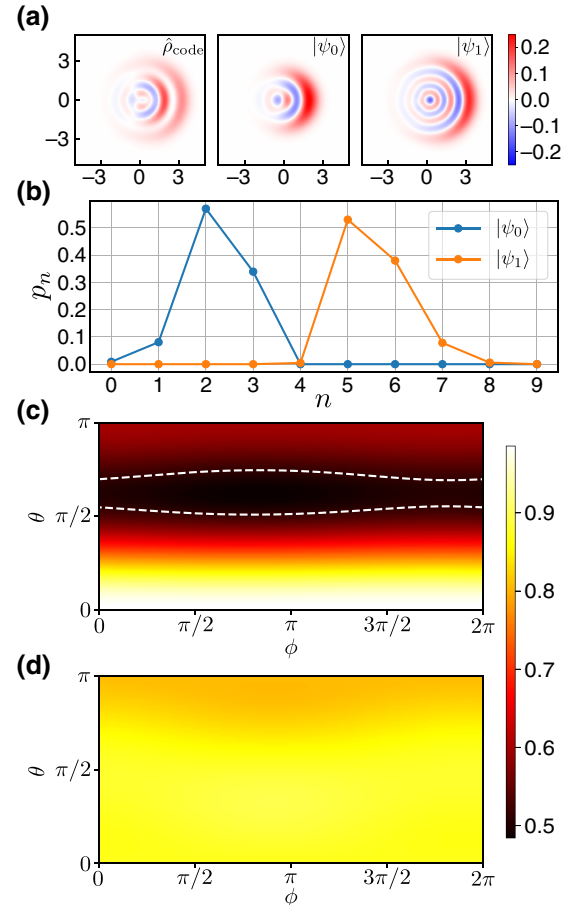


FIG. 5. (a),(b) Wigner functions and photon-number distributions for the discovered encoding in Fig. 2(c)ii. (c) Single-state fidelity $F_{\theta\phi}$ at $t = 10 \mu\text{s}$ for the whole Bloch sphere. The white dashed line indicates the break-even fidelity. (d) $F_{\theta\phi}$ on the Bloch sphere for the $\sqrt{3}$ code. For all Wigner function plots throughout this paper, the horizontal axis label is $x = (\hat{a} + \hat{a}^\dagger)/\sqrt{2}$ and the vertical axis label is $p = i(\hat{a}^\dagger - \hat{a})/\sqrt{2}$.

where $|\psi_0\rangle \in \{|1\rangle, |2\rangle, |3\rangle\}$ occupies only low photon-number states and $|\psi_1\rangle \in \{|5\rangle, |6\rangle, |7\rangle\}$ occupies only high photon-number states.

To understand how the logical subspace is preserved under the AQEC Hamiltonian, we plot the single-state fidelity $F_{\theta\phi}$ over the Bloch sphere [Fig. 5(c)] at $t = 10 \mu\text{s}$. The logical state $|\psi_0\rangle$ is strongly stabilized by the AQEC Hamiltonian with a fidelity 0.985 and $|\psi_1\rangle$ is preserved with a lower fidelity 0.598. Some of their superposition states (θ, ϕ in-between the white dashed line) have fidelities below break even, but the average fidelity over the whole Bloch sphere still exceeds break even [Fig. 2(e) red dashed line] due to the partial protection in the logical subspace. In comparison, we also plot the single-state fidelity for the $\sqrt{3}$ code [Fig. 2(c)i] in Fig. 5(d), which shows a relatively uniform protection for any logical states.

We could study a simplified example to demonstrate that a partially protected logical subspace exceeds break even. Stabilizing Fock states $|0\rangle$ and $|2\rangle$ under photon-loss error can be implemented with a distance 1 Hamiltonian $\hat{H} = |2, e\rangle\langle 1, g| + |1, g\rangle\langle 2, e|$. At long time, both logical states are stabilized with single-state fidelities $F_{\theta=0}(t) \approx F_{\theta=\pi}(t) \approx 1$ but any coherent superposition state becomes a complete mixture of $\{|0\rangle\langle 0|, |2\rangle\langle 2|\}$. This leads to an average fidelity of $2/3$, which is better than the break-even fidelity $1/2$. Intuitively, stabilizing both $|\psi_0\rangle$ and $|\psi_1\rangle$ preserves strictly more information compared to collapsing the whole Bloch sphere to $|\psi_0\rangle = |0\rangle$.

2. A different $\sqrt{3}$ code

Besides the $\sqrt{3}$ code explained in the main text, AutoQEC also discovered another variant of the $\sqrt{3}$ code [Fig. 6(a)] protected by a distance 2 Hamiltonian. The main difference is that $|\psi_1\rangle \in \{|1\rangle, |4\rangle, |7\rangle\}$ instead of $\{|1\rangle, |4\rangle, |6\rangle\}$ [Fig. 6(b)]. Following the same procedures as in Appendix C, this new code can also be analytically derived as [$F \approx 99.8\%$ compared to the numerical results

in Fig. 6(a)]

$$\begin{aligned} |\psi_0\rangle &= \sqrt{1 - \frac{1}{\sqrt{3}}} |0\rangle + \frac{1}{\sqrt{3}} |3\rangle, \\ |\psi_1\rangle &= \sqrt{\frac{4(7 - \sqrt{3})}{3(7 + \sqrt{3})}} |1\rangle - \sqrt{\frac{(\sqrt{3} - 1)(7 - \sqrt{3})}{3(7 + \sqrt{3})}} |4\rangle \\ &\quad + \sqrt{\frac{3 - \sqrt{3}}{3(7 + \sqrt{3})}} |7\rangle. \end{aligned} \quad (\text{F1})$$

3. Discovering the three-qubit bit-flip code

AutoQEC can also be applied to qubit-based systems and here we show a test example of discovering the three-qubit bit-flip code. More concretely, we choose three data qubits with dissipators $\{\sqrt{\kappa}\hat{X}_i, i = 1, 2, 3\}$, and two ancilla qubits with dissipators $\{\sqrt{\kappa_q}|g_i\rangle\langle e_i|, i = 4, 5\}$, since generally qubit-based systems have more errors and require more lossy ancilla states to evacuate the entropy from the system. The loss rates are fixed at $\kappa/2\pi = 0.1$ MHz and $\kappa_q/2\pi = 20$ MHz, and the total evolution time is $T = 0.2 \mu\text{s}$. We consider the all-to-all coupling Hamiltonian $\hat{H}_{\text{AQEC}} = \sum_{i=1}^N \sum_{j=i}^N \alpha_{ij} (|i\rangle\langle j| + |j\rangle\langle i|)$ where $N = 32$ is the total number of basis states $\{|i\rangle, i = 1, \dots, N\}$ for a five-qubit system. The control parameters α_{ij} (bounded by $|\alpha_{ij}|/2\pi \leq 100$ MHz) as well as the amplitudes of the logical states $\langle i|\psi_0\rangle$ and $\langle i|\psi_1\rangle$ are all forced to be real numbers in the optimization.

In Fig. 7(a), we show the wave functions of the discovered codes from four different runs, which all give average fidelity around 96.4% with a small standard deviation about 0.02%. The first code [Fig. 7(a)i] is similar to the usual repetition code while the remaining three codes look quite different from the repetition code. Notice that there are an infinite number of three qubit bit-flip codes and any one of them could lead to a valid AQEC Hamiltonian due to the all-to-all assumption.

To verify that all discovered encodings are indeed approximate QEC codes for the bit-flip channel, we plot the QEC matrix for each encoding in Fig. 7(b), which shows small deviations from the perfect quantum error correction criteria. Here the QEC matrix \mathcal{E} is defined as

$$\begin{aligned} \mathcal{E}_{2m+i, 2n+j} &= \text{Tr} \left[\hat{E}_m^\dagger \hat{E}_n \left(|\psi_j\rangle\langle\psi_i| - \frac{1}{2} \delta_{ij} (|\psi_i\rangle\langle\psi_i| + |\psi_j\rangle\langle\psi_j|) \right) \right], \end{aligned} \quad (\text{F2})$$

where $i, j \in \{0, 1\}$, $m, n \in \{0, 1, 2, 3\}$ and the operators are $\{\hat{E}_n\} = \{\hat{I}, \hat{X}_1, \hat{X}_2, \hat{X}_3\}$.

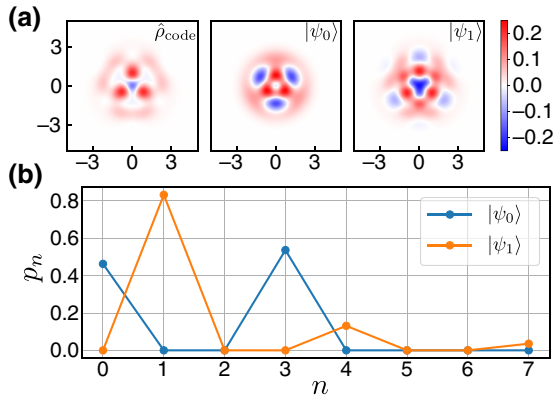


FIG. 6. (a),(b) Wigner functions and photon-number distributions for another variant of the $\sqrt{3}$ code discovered with $d = 2$ Hamiltonian.

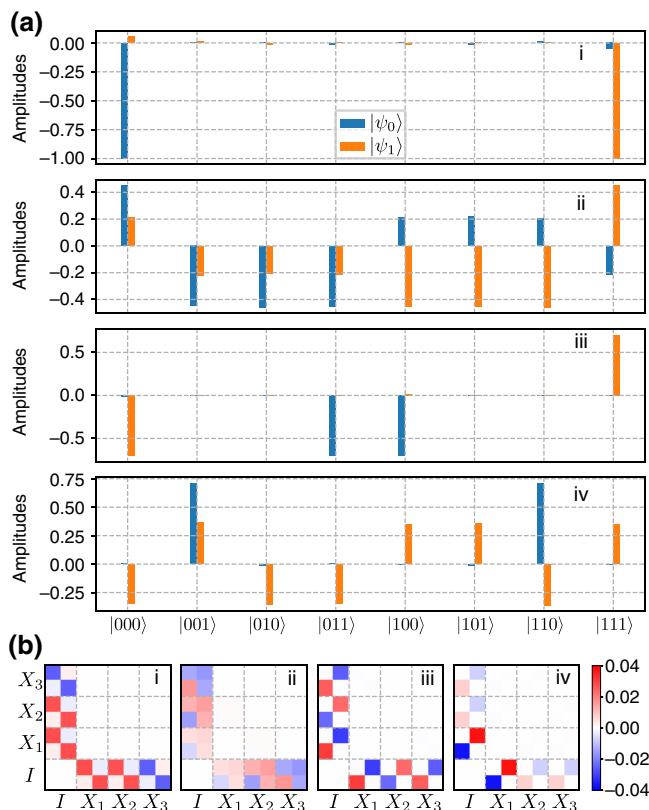


FIG. 7. (a) Discovered three qubit bit-flip codes from four different runs. (b) QEC matrix for each of the discovered encoding, representing deviations from the perfect QEC criteria.

APPENDIX G: TRAINING DETAILS

We use Adam optimizer [36] for the gradient-based learning with a learning rate about 0.001. Usually after a few hundred iterations, we can tell whether the training is stuck at a bad local minimum below break even or not and make a decision on early stops. The training often achieves good convergence after a few thousand iterations and we could lower the learning rate to about 0.0003 for the final learning stage.

Each AutoQEC run starts with randomly initializing both state vectors and the Hamiltonian parameters, and typically we have around 30 runs (including the early stopped ones) for each Hamiltonian setting in order to have enough results that exceed break even and to explore more of the solution space. With a Fock state cutoff at 20, the Hilbert-space dimension is 40 and the number of free parameters for the logical basis states $|\psi_0\rangle$ and $|\psi_1\rangle$ is $40 \times 4 = 160$. The total number of free parameters for the Hamiltonian depends on the Hamiltonian connectivity: 1600 for all-to-all coupling and 148 in the $d = 2$ case.

During the optimization, in general $|\psi_0\rangle$ and $|\psi_1\rangle$ would not be perfectly orthogonal to each other after an Adam update step and therefore we choose to maintain

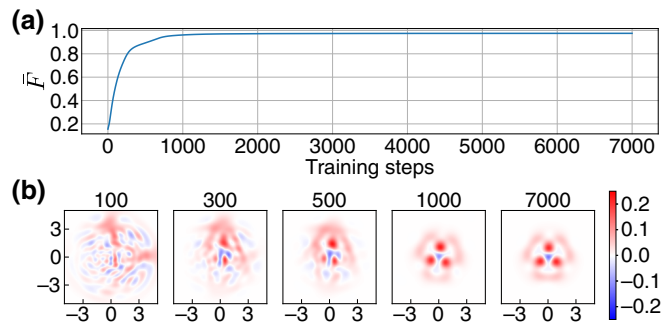


FIG. 8. (a) Learning curve for results in Fig. 6. (b) Wigner functions of $\hat{\rho}_{code}$ at different iterations during training, which shows a relatively good convergence after a few thousand iterations.

their orthogonality by manually setting $|\psi_1\rangle \rightarrow |\psi_1\rangle - \langle\psi_0|\psi_1\rangle/\langle\psi_0|\psi_0\rangle|\psi_0\rangle$ after each iteration. The constraints on the driving strength $|\alpha_j| \leq \alpha_{max}$ are ensured by optimizing over the angle variables θ_j defined as $\alpha_j = \alpha_{max} \cos \theta_j$ instead of α_j directly.

Figure 8 shows the learning curve for results in Fig. 6 discovered with $d = 2$ Hamiltonian. Similar learning curves occur frequently through many runs of AutoQEC. Regarding computational cost, each iteration takes about 12 s on three CPUs (Intel Xeon CPU E5-2609 v4 @ 1.70GHz) for training with distance two Hamiltonians. AutoQEC runs on three CPUs because $\hat{\rho}_{00}(t)$, $\hat{\rho}_{11}(t)$, $\hat{\rho}_{10}(t)$ in the definition of $\bar{F}(t)$ can be evaluated in parallel with three independent master equation time evolutions.

-
- [1] M. A. Nielsen and I. L. Chuang, *Quantum Computation and Quantum Information* (Cambridge University Press, Cambridge, 2010).
 - [2] N. Ofek, A. Petrenko, R. Heeres, P. Reinhold, Z. Leghtas, B. Vlastakis, Y. Liu, L. Frunzio, S. M. Girvin, L. Jiang, M. Mirrahimi, M. H. Devoret, and R. J. Schoelkopf, Extending the lifetime of a quantum bit with error correction in superconducting circuits, *Nature* **536**, 441 (2016).
 - [3] L. Hu, Y. Ma, W. Cai, X. Mu, Y. Xu, W. Wang, Y. Wu, H. Wang, Y. P. Song, C. L. Zou, S. M. Girvin, L. M. Duan, and L. Sun, Quantum error correction and universal gate set operation on a binomial bosonic logical qubit, *Nat. Phys.* **15**, 503 (2019).
 - [4] P. Campagne-Ibarcq, A. Eickbusch, S. Touzard, E. Zaly-Geller, N. E. Frattini, V. V. Sivak, P. Reinhold, S. Puri, S. Shankar, R. J. Schoelkopf, L. Frunzio, M. Mirrahimi, and M. H. Devoret, Quantum error correction of a qubit encoded in grid states of an oscillator, *Nature* **584**, 368 (2020).
 - [5] A. G. Fowler, M. Mariantoni, J. M. Martinis, and A. N. Cleland, Surface codes: Towards practical large-scale quantum computation, *Phys. Rev. A - At., Mol., Opt. Phys.* **86**, 032324 (2012).

- [6] B. M. Terhal, Quantum error correction for quantum memories, *Rev. Mod. Phys.* **87**, 307 (2015).
- [7] E. Kapit, Hardware-Efficient and Fully Autonomous Quantum Error Correction in Superconducting Circuits, *Phys. Rev. Lett.* **116**, 150501 (2016).
- [8] F. Reiter, A. S. Sørensen, P. Zoller, and C. A. Muschik, Dissipative quantum error correction and application to quantum sensing with trapped ions, *Nat. Commun.* **8**, 1822 (2017).
- [9] J. M. Gertler, B. Baker, J. Li, S. Shirol, J. Koch, and C. Wang, Protecting a bosonic qubit with autonomous quantum error correction, *Nature* **590**, 243 (2021).
- [10] J. Lebreuilly, K. Noh, C.-H. Wang, S. M. Girvin, and L. Jiang (2021), [ArXiv:2103.05007](https://arxiv.org/abs/2103.05007).
- [11] J. Kerckhoff, H. I. Nurdin, D. S. Pavlichin, and H. Mabuchi, Designing Quantum Memories with Embedded Control: Photonic Circuits for Autonomous Quantum Error Correction, *Phys. Rev. Lett.* **105**, 040502 (2010).
- [12] D. W. Leung, M. A. Nielsen, I. L. Chuang, and Y. Yamamoto, Approximate quantum error correction can lead to better codes, *Phys. Rev. A - At., Mol., Opt. Phys.* **56**, 2567 (1997).
- [13] M. Reimpell and R. F. Werner, Iterative Optimization of Quantum Error Correcting Codes, *Phys. Rev. Lett.* **94**, 080501 (2005).
- [14] A. S. Fletcher, P. W. Shor, and M. Z. Win, Channel-adapted quantum error correction for the amplitude damping channel, *IEEE Trans. Inf. Theory* **54**, 5705 (2008).
- [15] R. L. Kosut and D. A. Lidar, Quantum error correction via convex optimization, *Quantum Inf. Process.* **8**, 443 (2009).
- [16] T. Fösel, P. Tighineanu, T. Weiss, and F. Marquardt, Reinforcement Learning with Neural Networks for Quantum Feedback, *Phys. Rev. X* **8**, 031084 (2018).
- [17] P. D. Johnson, J. Romero, J. Olson, Y. Cao, and A. Aspuru-Guzik (2017), [ArXiv:1711.02249](https://arxiv.org/abs/1711.02249).
- [18] Z. Chen, *et al.*, Measuring and Suppressing Quantum State Leakage in a Superconducting Qubit, *Phys. Rev. Lett.* **116**, 020501 (2016).
- [19] L. Pontryagin, *Mathematical Theory of Optimal Processes* (2018).
- [20] R. T. Chen, Y. Rubanova, J. Bettencourt, and D. Duvenaud, Neural ordinary differential equations, *Adv. Neural Inf. Process. Syst.* **2018-Decem**, 6571 (2018).
- [21] D. Gottesman, A. Kitaev, and J. Preskill, Encoding a qubit in an oscillator, *Phys. Rev. A. At., Mol., Opt. Phys.* **64**, 123101 (2001).
- [22] Z. Leghtas, G. Kirchmair, B. Vlastakis, R. J. Schoelkopf, M. H. Devoret, and M. Mirrahimi, Hardware-Efficient Autonomous Quantum Memory Protection, *Phys. Rev. Lett.* **111**, 120501 (2013).
- [23] M. H. Michael, M. Silveri, R. T. Brierley, V. V. Albert, J. Salmilehto, L. Jiang, and S. M. Girvin, New Class of Quantum Error-Correcting Codes for a Bosonic Mode, *Phys. Rev. X* **6**, 031006 (2016).
- [24] V. V. Albert, K. Noh, K. Duivenvoorden, D. J. Young, R. T. Brierley, P. Reinhold, C. Vuillot, L. Li, C. Shen, S. M. Girvin, B. M. Terhal, and L. Jiang, Performance and structure of single-mode bosonic codes, *Phys. Rev. A* **97**, 032346 (2018).
- [25] A. M. Steane, Error Correcting Codes in Quantum Theory, *Phys. Rev. Lett.* **77**, 793 (1996).
- [26] J. Guillaud and M. Mirrahimi, Repetition Cat Qubits for Fault-Tolerant Quantum Computation, *Phys. Rev. X* **9**, 041053 (2019).
- [27] F. Reiter and A. S. Sørensen, Effective operator formalism for open quantum systems, *Phys. Rev. A - At., Mol., Opt. Phys.* **85**, 032111 (2012).
- [28] D. F. James and J. Jerke, Effective Hamiltonian theory and its applications in quantum information, *Can. J. Phys.* **85**, 625 (2007).
- [29] Y. Zhang, J. C. Curtis, C. S. Wang, R. J. Schoelkopf, and S. M. Girvin (2021), [ArXiv:2106.09112](https://arxiv.org/abs/2106.09112).
- [30] M. Reagor, W. Pfaff, C. Axline, R. W. Heeres, N. Ofek, K. Sliwa, E. Holland, C. Wang, J. Blumoff, K. Chou, M. J. Hatridge, L. Frunzio, M. H. Devoret, L. Jiang, and R. J. Schoelkopf, Quantum memory with millisecond coherence in circuit QED, *Phys. Rev. B* **94**, 014506 (2016).
- [31] P. Arrangoiz-Arriola, E. A. Wollack, Z. Wang, M. Pechal, W. Jiang, T. P. McKenna, J. D. Witmer, R. Van Laer, and A. H. Safavi-Naeini, Resolving the energy levels of a nanomechanical oscillator, *Nature* **571**, 537 (2019).
- [32] G. S. MacCabe, H. Ren, J. Luo, J. D. Cohen, H. Zhou, A. Sipahigil, M. Mirhosseini, and O. Painter, Nano-acoustic resonator with ultralong phonon lifetime, *Science* **370**, 840 (2020).
- [33] R. Lescanne, M. Villiers, T. Peronnin, A. Sarlette, M. Delbecq, B. Huard, T. Kontos, M. Mirrahimi, and Z. Leghtas, Exponential suppression of bit-flips in a qubit encoded in an oscillator, *Nat. Phys.* **16**, 509 (2020).
- [34] J. R. Johansson, P. D. Nation, and F. Nori, QuTiP: An open-source python framework for the dynamics of open quantum systems, *Comput. Phys. Commun.* **183**, 1760 (2012).
- [35] J. R. Johansson, P. D. Nation, and F. Nori, QuTiP 2: A python framework for the dynamics of open quantum systems, *Comput. Phys. Commun.* **184**, 1234 (2013).
- [36] D. P. Kingma and J. L. Ba, *3rd International Conference on Learning Representations, ICLR 2015 - Conference Track Proceedings* (2015).